A MULTISCALE HYBRID MODEL FOR PRO-ANGIOGENIC CALCIUM SIGNALS IN A VASCULAR ENDOTHELIAL CELL

MARCO SCIANNA[A,B,1]

[A] Department of Mathematics, Politecnico di Torino, Corso Duca degli Abruzzi 24, 10129 Torino, Italy

[B] Institute for Cancer Research, University of Torino Medical School, Strada Provinciale 142, 10060 Candiolo, Italy

Abstract

CYTOSOLIC CALCIUM MACHINERY IS ONE OF THE PRINCIPAL SIGNALLING MECHANISMS BY WHICH ENDOTHELIAL CELLS (ECS) RESPOND TO EXTERNAL STIMULI DURING SEVERAL BIOLOGICAL PROCESSES, INCLUDING VASCULAR PROGRESSION IN BOTH PHYSIOLOGICAL AND PATHOLOGICAL CONDITIONS. LOW CONCENTRATIONS OF ANGIOGENIC FACTORS (SUCH AS VEGF) ACTIVATE IN FACT COMPLEX PATHWAYS INVOLVING, AMONG OTHERS, SECOND MESSENGERS ARACHIDONIC ACID (AA) AND NITRIC OXIDE (NO), WHICH, IN TURN, CONTROL THE ACTIVITY OF PLASMAMEMBRANE CALCIUM CHANNELS. THE SUBSEQUENT INCREASE IN THE INTRACELLULAR LEVEL OF THE ION REGULATES FUNDAMENTAL BIOPHYSICAL PROPERTIES OF ECS (SUCH AS ELASTICITY, INTRINSIC MOTILITY, AND CHEMICAL STRENGTH), ENHANCING THEIR MIGRATORY CAPACITY. PREVIOUSLY, A NUMBER OF CONTINUOUS MODELS HAVE REPRESENTED CYTOSOLIC CALCIUM DYNAMICS, WHILE EC MIGRATION IN ANGIOGENESIS HAS BEEN SEPARATELY APPROACHED WITH DISCRETE, LATTICE-BASED TECHNIQUES. THESE TWO COMPONENTS ARE HERE INTEGRATED AND INTERFACED TO PROVIDE A MULTISCALE AND HYBRID CELLULAR POTTS MODEL (CPM), WHERE THE PHENOMENOLOGY OF A MOTILE EC IS REALISTICALLY MEDIATED BY ITS CALCIUM-DEPENDENT SUBCELLULAR EVENTS. THE MODEL, BASED ON A REALISTIC 3-D CELL MORPHOLOGY WITH A NUCLEAR AND A CYTOSOLIC REGION, IS SET WITH KNOWN BIOCHEMICAL AND ELECTROPHYSIOLOGICAL DATA. IN PARTICULAR, THE RESULTING SIMULATIONS ARE ABLE TO REPRODUCE AND DESCRIBE THE POLARIZATION PROCESS, TYPICAL OF STIMULATED VASCULAR CELLS, IN VARIOUS EXPERIMENTAL CONDITIONS. MOREOVER, BY ANALYZING THE MUTUAL INTERACTIONS BETWEEN MULTILEVEL BIOCHEMICAL AND BIOMECHANICAL ASPECTS, OUR STUDY INVESTIGATES WAYS TO INHIBIT CELL MIGRATION: SUCH STRATEGIES HAVE IN FACT THE POTENTIAL TO RESULT IN PHARMACOLOGICAL INTERVENTIONS USEFUL TO DISRUPT MALIGNANT VASCULAR PROGRESSION.

KEYWORDS: CELLULAR POTTS MODEL · MULTISCALE MODEL · VASCULAR ENDOTHELIAL GROWTH FACTOR · CALCIUM.

[1] CORRESPONDING AUTHOR. E-MAIL: marcosci1@alice.it

1 Introduction

Finely tuned spatio-temporal calcium events are a highly conserved and ubiquitous mode for the control of biochemistry and physiology in almost all eukaryotic cells [12, 15, 20]. Endothelial cells (ECs) are no exception, and intracellular calcium serves as a positive or negative regulatory signal for a wide range of cell functions, including survival, proliferation, motility, apoptosis and differentiation [11, 13, 68]. A broad number of calcium-dependent enzymes are also associated with the progression through the cell cycle (the exit from quiescence in early G1 phase, the G1/S transition and other checkpoints during S and M phases [5, 43, 72]), and mediate the activation of several nuclear factors involved in the DNA division machinery, for example cdk and cyclins [22, 25, 87].

Under resting conditions, different control mechanisms maintain the concentration of free cytosolic calcium very low, nearly 10^{-7} M, with respect to the extracellular environment and to intracellular compartments (primarily the endoplasmic reticulum, ER [1, 86, 94]). In particular, the ion is extruded from the cytosol by calcium pumps, which are present in both plasma and ER membranes (respectively PMCA and SERCAs) and directly consume ATP energy, and by Na-Ca exchangers, which are located only in the plasmamembrane and use the energy of Na^+ electrochemical gradients [35, 40, 100]. On the other hand, calcium enters into the cytosol through permeable channels sited within the different membranes and activated by intracellular messengers [10, 54, 77].

The correct Ca^{2+} concentration is thus strictly regulated by these active and passive fluxes. Alterations of this fine balance can be triggered only by specific extracellular agonists, and are typical chemical signals transducing information during several biological processes, including new vascular progression in both physiological (such as vascularization of ovary and uterus during the menstrual cycle, of mammary glands during lactation and of granulation tissue after wound healing) and pathological (for example chronic inflammatory diseases, vasculopathies, degenerative disorders, tissue injury occurring in ischemia or tumor progression) conditions [17, 74, 80]. In particular, vascular endothelial growth factors, VEGFs, which act as a positive chemotactic guidance for ECs (as widely demonstrated in literature [16, 18, 103]), concomitantly mediate several calcium-dependent pathways. As characterized in [28, 45, 67, 68, 73, 98], VEGF molecules, binding to their surface tyrosine kinase receptors, initiate in fact a series of intracellular cascades, which results in the indirect production of arachidonic acid (AA) and nitric oxide (NO). Both these second messengers bind to sites on plasmamembrane, opening cation channels and thus allowing the influx of extracellular calcium into the cytosol, see Fig. 2. The process, also called non-capacitive (or non-store-operated) calcium entry (NCCE or NSOCE), causes a localized and peripheral restricted accumulation of the ion [98], and regulates important biophysical properties of ECs, such as their intrinsic motility, elasticity and chemotactic strength, ultimately enhancing their migratory capacity, which is fundamental in the initial phases of the vascular progression [9, 27, 29].

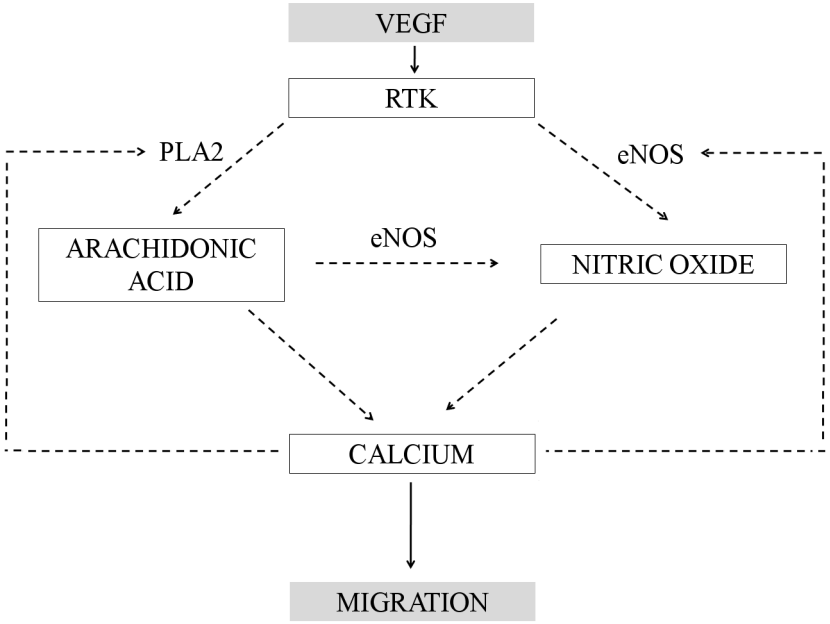

Figure 1: Simplified schematic representation of VEGF-induced calcium-dependent events during chemotactic migration of a vascular endothelial cell. VEGF molecules, binding to tyrosine kinase receptors, activate a series of intracellular signalling inducing the recruitment of enzymes phospholipases A2 (PLA2) and nitric oxide synthase (eNOS), and the subsequent production of arachidonic acid (AA) and nitric oxide (NO). Both these second messengers mediate calcium influxes from the extracellular environment through plasmamembrane channels. Increases in cytosolic calcium level influence the migratory capacity of the EC. The dashed arrows stand for indirect reactions, which are bundled in the model. Such scheme is based on [68, 67, 98]

The aim of this work is to systematically characterize the interactions between these multilevel biochemical and biomechanical mechanisms, and investigate their effects on the phenomenology of a vascular cell. Individually, each component has been previously considered: a number of continuous microscopic models have in fact characterized calcium dynamics in different cell types [26, 42, 49, 93, 94], while several discrete cell-level CPMs have treated the motion of vascular endothelial cells during angiogenesis [6, 56] or vasculogenesis [3, 60, 61, 62]. We here interface and integrate such different approaches to assemble a unique multiscale model: it simulates a simple and reliable motility assay with an endothelial cell placed on one side of a three-dimensional chamber and stimulated by an exogenous VEGF source. In particular, at the lowest molecular level, we use an adapted version of the work of L. Munaron [75], which, basing on experimental evidences (mainly patch clamp and single cell fluorescence microscopy provided by his group), has been able to accurately reproduce the basic properties of proangiogenic calcium signals in a static EC. Next, at the cellular level, we introduce a Cellular Potts Model (CPM), developed for instance in [4, 33, 34, 36, 57], to describe the 3-D EC morphology, strictly based on experimental images and characterized by a realistic differentiation between the nucleus and the cytosolic region, and its phenomenology. As a key ingredient of our hybrid framework, the subcellular calcium biochemistry is coordinated to realistically deliver the mesoscopic cell properties, described

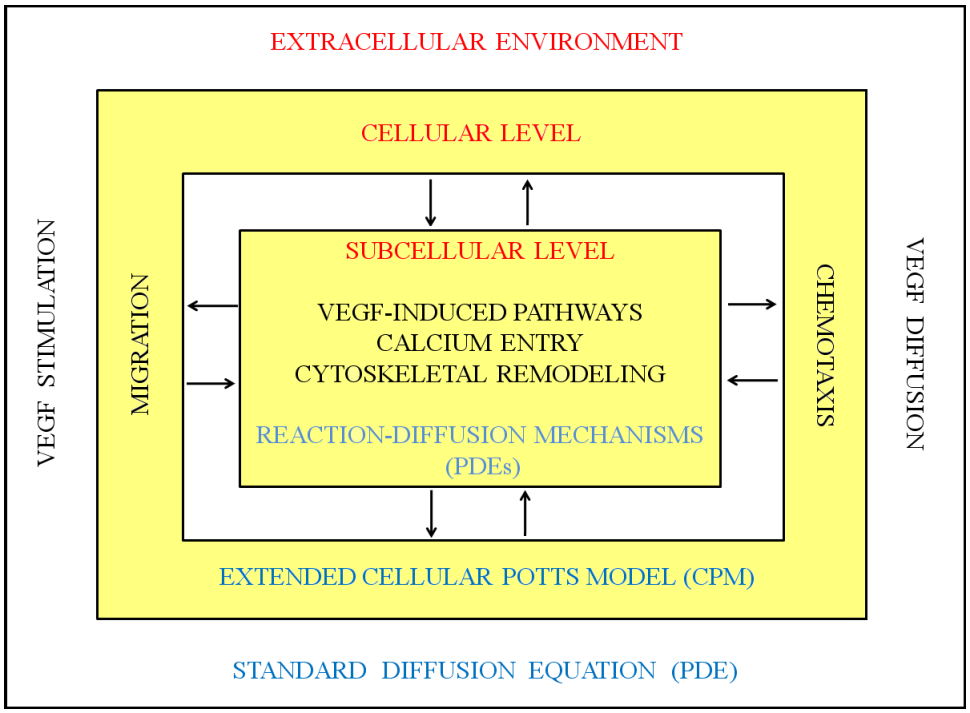

Figure 2: Hierarchy of scales and environments, and corresponding biological mechanisms and modeling approaches. Information flows from microscopic intracellular biochemical processes to the mesoscopic cell-level phenomenology.

by typical Potts parameters. The resulting model, utilizing the advantage of both discrete and continuous techniques, is thus able to span all the different biological spatio-temporal scales involved, which range from 10^{-8} m and 10^{-9} s for the intracellular molecular processes to 10^{-6} m and hours for the cell-level phenomenology, which directly impact each other.

The model simulations reproduce the varying morphologies of a motile vascular cell, while characterizing the VEGF-induced calcium events, in a good agreement with experimental measurements. We further find close quantitative relations between such intracellular Ca^{2+} dynamics and the cell migratory parameters (such as velocity and mean displacement) under different physiopathological conditions. In particular, we focus on the model counterparts of biomedical approaches which, interfering with calcium machinery, are able to slow down cell migration: such strategies, in fact, may represent useful pharmacological treatments that have the potential to disrupt malignant neovascularization.

2 Mathematical Model

The continuous approach describing the VEGF evolution and its downstream signalling, and the discrete Cellular Potts model phenomenologically reproducing the migration of the endothelial cell are integrated to produce a hybrid system. In particular, the microscopic dynamics of intracellular calcium alter mesoscopic biophysical properties of the ECs, such as its motility, compressibility and chemotactic strength, ultimately affecting its behavior. Thus all levels of the model are explicitly integrated and feed back over the whole simulation.

2.1 Extended Cellular Potts Model

The Cellular Potts Model is a grid-based stochastic approach, which describes the evolution of the simulated system in terms of effective energies and constraints. To represent biological systems, the CPM uses a numerical lattice, where each site $\mathbf{x}$ is identified by an integer index, a degenerate *spin* $\sigma(\mathbf{x}) \in \mathbb{N}$. Typically, each cell is an undifferentiated domain of contiguous voxels with the same spin, whereas cell membranes are the borders between voxels with different spins. In this work, we use a more realistic extension of the CPM (see the Discussion for a detailed comment): the vascular endothelial cell is differentiated in a nuclear and a cytosolic region, which are classical CPM domains. In particular, the sites $\mathbf{x}$ belonging to the nucleus have spin $\sigma(\mathbf{x}) = 1$, those of the cytosol $\sigma(\mathbf{x}) = 2$. The plasma and the nuclear envelopes are defined as the borders between the cytosolic compartment and, respectively, the medium and the nuclear region, see Fig. 3A. Initially the EC is an hemisphere of 30 μm in length and width and of 15 μm in height, while the nucleus, whose location and geometry is estimated from experimental images, is a sphere of 10 μm of diameter, as depicted in Fig. 3B: these measures agree with the most usual morphologies observed in classical cultures for resting ECs in the presence of adequate nutrients and the absence of external forces [27, 98]. We further define a special generalized cell $\sigma = 0$ representing the extracellular medium. It is assumed to be static, passive and homogenously distributed throughout the three-dimensional simulation domain, forming no large-scale structures and thus without volume or surface constraints, as done in [60, 61].

Instead of directly representing the forces that act on the simulated environment, the CPM aggregates them into a functional, the Hamiltonian H. It contains a variable number of terms, such as cell attributes (e.g., volume, surface) and effective energies (e.g., cell response to chemotactic stimulus). The cell motion comes from the overall minimization of H through stochastic fluctuations. The core algorithm is Metropolis method for Monte Carlo dynamics [36, 64]. Procedurally, a lattice site (*source site*, $\mathbf{x}_{source}$) is selected at random and assigns its spin state ($\sigma(\mathbf{x}_{source})$) to one of its unlike neighbors (*target site*, $\mathbf{x}_{target}$), which has also been randomly selected. Such a proposed change in the lattice configuration is called *spin copy*. The Hamiltonian of the system is computed before and after the proposed

0	0	0	0	0	0	0	0	0
0	0	2	2	2	2	2	0	0
0	2	2	2	2	2	2	2	0
0	2	2	1	1	1	2	2	0
0	2	2	1	1	1	2	2	0
0	2	2	1	1	1	2	2	0
0	2	2	2	2	2	2	2	0
0	0	2	2	2	2	2	0	0
0	0	0	0	0	0	0	0	0

(A)

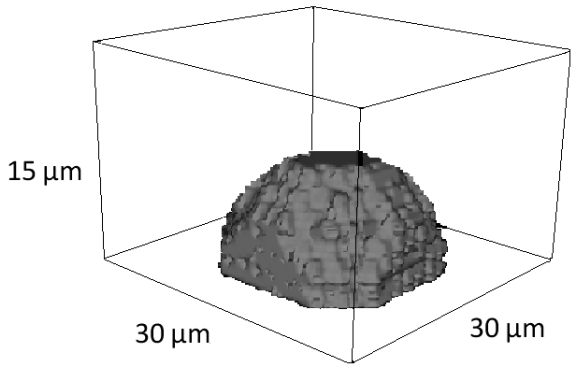

(B)

Figure 3: (A) A typical CPM grid and representation of a compartmentalized cell. Lattice sites of the nuclear region ($\sigma(\mathbf{x}) = 1$) are in yellow, lattice sites of the cytosol in grey ($\sigma(\mathbf{x}) = 2$). The extracellular medium is labeled with $\sigma(\mathbf{x}) = 0$. (B) Representation of the initial 3-D morphology of the simulated vascular EC, which is 30 μm in length and width and about 15 μm in height. (B)

update: if H is reduced as the result of the copy (e.g. the copy is energetically favourable), the change is accepted, else the Boltzmann probability

$$P(\Delta H > 0)(t) = e^{-\Delta H / T_{\sigma(\mathbf{x}_{source})}(t)} \tag{2.1}$$

is used, where $T_{\sigma(\mathbf{x}_{source})}$ is an effective Boltzmann temperature of the moving site $\mathbf{x}_{source}$. A total of n proposed updates, where n is the number of sites of the lattice, constitutes a Monte Carlo Step (MCS), which is the basic iteration and the unit of time used in the model. If $\sigma(\mathbf{x}_{source}) = 1$, $T_{\sigma(\mathbf{x}_{source})} = T_1$ is a low constant positive value and mimics the passive motion of the cell nucleus, which is dragged by the surrounding cytosolic region (we remainder the reader to Sec. 3 for a more complete discussion). Instead, if $\sigma(\mathbf{x}_{source}) = 2$, $T_{\sigma(\mathbf{x}_{source})}$ gives a measure of the frequency of the biased extensions and retractions of cell plasmamembrane, which result from the non-equilibrium state between outward and inward forces. Such an intrinsic motility, the primary driving force of cell non-directional movements, is mediated by the overall intracellular calcium level in a dose dependent manner, as provided in [29], where wound healing assays are performed on several types of vascular cells stimulated by different agonists (such as AA and NO themselves). We therefore use a Michaelis-Menten law:

$$T_{\sigma(\mathbf{x}_{source}):\sigma(\mathbf{x}_{source})=2}(t) = T_0 \left[\frac{1 + \widetilde{Ca}(t)}{1 + h\widetilde{Ca}(t)} \right], \tag{2.2}$$

where, here and in the following, **the rate of intracellular calcium accumulation** $\widetilde{Ca}(t) = [Ca(t)/C_0] - 1$ is a

positive value, since $Ca(t) = \sum_{\mathbf{x}:\sigma(\mathbf{x})\in\{1,2\}} Ca(\mathbf{x},t)$ corresponds to the total concentration of the ion at time t, and $C_0 = \sum_{\mathbf{x}:\sigma(\mathbf{x})\in\{1,2\}} Ca_0$ is its total basal level (the level below which the cell dies, for its estimation see Table III and the Appendix). Hence T_0 corresponds to the basal motility of the cell (i.e., in resting conditions at the basal calcium level Ca_0), and T_0/h to the asymptotic value (i.e., for saturating concentrations of the ion).

The hamiltonian of the system, whose minimization, as seen, drives the cell phenomenology is:

$$H = H_{shape} + H_{adhesion} + H_{chemical} + H_{persitence}. \tag{2.3}$$

H_{shape} takes into account of the cell shape growth and deformation, which are described with an elastic-like term:

$$H_{shape}(t) = H_{volume}(t) + H_{surface}(t) = \mu_1(v_1(t) - V_1)^2 + \mu_2(v_2(t) - V_2)^2 + \lambda_1(s_1(t) - S_1)^2 + \lambda_2(t)(s_2(t) - S_2)^2, \tag{2.4}$$

where v_i and s_i, with $i \in \{1,2\}$, are, respectively, the actual volume and surface of the two cell compartments, and V_i and S_i are their initial measures. μ_i and λ_i are penalty coefficients controlling, respectively, the size and the elasticity of the subunits' membranes (i.e., deviation of v_i and s_i from V_i and S_i increase the functional H). Since we do not include in the model the addition of any types of nutrient (such as oxygen), the cell volume fluctuations are kept negligible, within a few percent, by high values for μ_1 and μ_2, as done in similar theoretical works [60]. Moreover, because of cell nuclei do not strongly deform, we set high a high value also for λ_1. λ_2 is instead a measure of the ease with which the EC changes its shape due to cytoskeletal remodeling (i.e., it is a sort of inverse of its compressibility). Following [9], where has been provided the fact that actin-myosin interactions and reorganizations are facilitated by the presence of free calcium ions, we set

$$\lambda_2(t) = \lambda_{2,0} \ \exp\left(-k\widetilde{Ca}(t)\right), \tag{2.5}$$

where $\lambda_{2,0}$ is the intrinsic cell resistance to compression at the basal calcium concentration Ca_0. In particular, for saturating levels of Ca^{2+}, $\lambda_2 \to 0$, and the cell can undergo a dramatic change in its morphology in response to the external stimulus.

$H_{adhesion}$ is the energy contribution due the generalized adhesion between the nuclear and the cytosolic compartments, which is a general extension of the Steimberg's differential adhesion hypothesis (DAH) [36, 95, 96]:

$$H_{adhesion}(t) = \sum_{\mathbf{x},\mathbf{x}'} J_{1,2}(1 - \delta_{\sigma(\mathbf{x}),\sigma(\mathbf{x}')}(t)), \tag{2.6}$$

where $\mathbf{x}$, $\mathbf{x}'$ represent two neighboring lattice sites within the cell and $\delta_{x,y} = \{1, x = y; 0, x \neq y\}$ is the Kronecher delta. We prevent the cell to split into disconnected patches by assigning a large negative energy penalty $J_{1,2}$.

Since vascular EC have been demonstrated to migrates along gradients of VEGF concentration [32, 92], we add a linear-type chemotaxis term to the effective energy [88]:

$$\Delta H_{chemotaxis} = \mu_{ch}(\mathbf{x}_{source}, t) \left[Q(\mathbf{x}_{target}, t) - Q(\mathbf{x}_{source}, t) \right]. \tag{2.7}$$

$\mathbf{x}_{source}$ and $\mathbf{x}_{target}$ are, respectively, the source and the final lattice sites randomly selected during a trial update in a MCS: obviously, $\mathbf{x}_{source}$ is a cell membrane site while $\mathbf{x}_{target}$ is a medium site. The parameter μ_{ch} represents the local chemotactic sensitivity of the cell and evolves according to a Michaelis-Menten function:

$$\mu_{ch}(\mathbf{x}_{source}, t) = \mu_{ch,0} \left[\frac{1 + Ca(\mathbf{x}_{source}, t)}{1 + jCa(\mathbf{x}_{source}, t)} \right], \tag{2.8}$$

where $\mu_{ch,0}$ is a basal chemotactic sensitivity. With this relation, we model the experimental evidence that the local redistribution of VEGF receptors from the Golgi apparatus to the plasmamembrane, and their following activation, is caused by a local elevation of cytosolic calcium ions [65]. Q is a measure of the local extracellular VEGF concentration sensed by the moving membrane site:

$$Q(\mathbf{x}, V) = \sum_{\mathbf{x}'} V(\mathbf{x}', t), \tag{2.9}$$

where $\mathbf{x} \in \{\mathbf{x}_{source}, \mathbf{x}_{target}\}$, and $\mathbf{x}'$ are all the matrix first-nearest neighbors of $\mathbf{x}$. Such a spatial approximation is in agreement with experimental results given in [32], where a direct chemotactic guidance by VEGF has been provided to require the existence of precisely shaped extracellular gradients in the close proximity of the cell surfaces. The local characterization of cell chemical response is a key feature of the model with respect to similar published works, where the chemotactic force is homogeneous within the cells' membranes [60, 61].

Besides the directional chemotactic migration, real vascular cells are seen to have a persistent motion dictated by their longer axes. It is a consequence of their polarization, i.e. their differentiation in a leading and a trailing surfaces. This inertial, shape-dependent motion is modeled with a further energy term, which coherently is a running mean over the cell past movements [4, 89]:

$$H_{persistence} = \mu_{pers}(t) ||\mathbf{v}(t) - \mathbf{v}(t - \Delta t)||^2, \tag{2.10}$$

where $\mathbf{v}(t) = \frac{\mathbf{x}_{CM}(t) - \mathbf{x}_{CM}(t - \Delta t)}{\Delta t}$ is the instantaneous velocity of the cell center of mass, as $\mathbf{x}_{CM}(t) = \frac{\sum_{\mathbf{x}:\sigma(\mathbf{x})=1,2} \mathbf{x}}{v_1(t) + v_2(t)}$,

and $\Delta t = 60$ MCS. μ_{pers} controls the persistence time and is:

$$\mu_{pers}(t) = \mu_{pers,0}\left[\frac{L(t)}{L_0} - 1\right], \tag{2.11}$$

where L is the current length of the longer axis of the cell, which is approximated with an ellipsoid, and L_0 is its initial value (the initial cell diameter). Obviously $L \geq L_0$, since we have assumed that the cell deforms but does not grow during patterning. Eq. (2.11) is based on the experimental evidence provided in [41], where after analogous chemical stimulations, elongated vascular cells have seen to have a longer persistence time than more rounded cells. This is explained with the observation that cell polarization is a cytoskeleton-driven process: the more a cell is polarized (i.e., the longer is its main axes), the more its actin filaments are in fact oriented in such a direction, requiring a longer time to reorient into a new direction, and thus to change the direction of motion of the whole cell. Coherently, from (2.11), if $\mu_{pers} = 0$ the EC undergoes uncorrelated Brownian motion, while if μ_{pers} is very large its motion is almost ballistic.

TABLE I - PARAMETERS INVOLVED IN THE MODEL

PARAMETER	DESCRIPTION	MODEL VALUE	REFERENCE
V_1	volume of nuclear compartment	900 [μm^3]	[98]
S_1	perimeter of nuclear compartment	314 [μm^2]	[98]
V_2	area of cytosolic compartment	32000 [μm^2]	[98]
S_2	perimeter of cytosolic compartment	1110 [μm^2]	[98]
T_0	basal EC motility	3.5	fit to experiments in [81]
T_1	generalized motility of the nucleus	0.25	
h	Michaelis-Menten coefficient for T	1/2	
μ_1	volume elasticity of nuclear compartment	20	
μ_2	volume elasticity of cytosolic compartment	20	
λ_1	surface elasticity of nuclear compartment	20	
$\lambda_{2,0}$	intrinsic plasma membrane elasticity	1.2	
k	Michaelis-Menten coefficient for λ_2	1	
J_{12}	generalized nucleus-cytosol adhesion within the same cell	-20	
$\mu_{ch,0}$	basal chemotactic strength	0.2	
j	Michaelis-Menten coefficient for μ_{ch}	1/2	
$\mu_{pers,0}$	basal inertia strength	0.8	fit to experiments in [81]

2.2 Modelling the VEGF-Mediated Calcium-Dependent Intracellular Events

The key biochemical processes incorporated in the model of the VEGF-induced calcium dynamics are as follows (see Fig. 4 for a diagrammatic representation):

- the exogenous VEGF diffuses throughout the extracellular medium, where it decays in a finite time;

- single molecules of morphogen reversibly combine with their tyrosine kinase receptors on cell surface, to form receptor-ligand complexes. These complexes decompose into a free receptor (which is recycled back) and some products, that initiate a sequence of reactions (i.e., the activation of enzymes PLA2 and eNOS) culminating in the production in the sub-plasmamemrane regions of second messengers AA and NO [30, 45, 68, 98];
- AA and NO open the relative and independent calcium channels in the plasma membrane, leading to extracellular calcium entry into the cytosol. The rates of calcium influx are increasing and saturating functions of AA and NO concentration, respectively [27, 28, 67, 71, 73, 98];
- NO release is further mediated by AA itself within cell cytosol [67, 68, 105];
- calcium enhance the rates of cytosolic AA and NO biosynthesis, with a positive feedback mechanism [53, 67, 68];
- calcium ions, which are reversibly buffered to proteins such as calmodium or to mitochondria [8, 10, 46, 51], are extruded from of the cell by plasmamembrane ATPase and Ca^{2+}-Na^{+} exchangers [35, 40, 100].

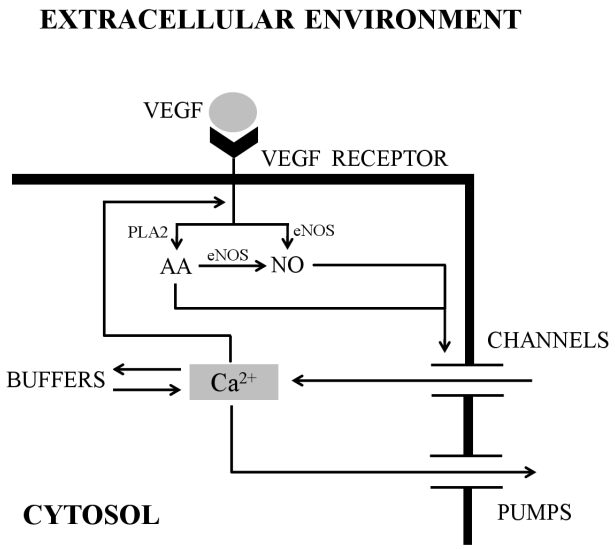

Figure 4: Diagram of the key VEGF-induced intracellular Ca^{2+} processes included in the mathematical model. Cell surface receptors activated by VEGF molecules stimulate the biosynthesis of AA and NO which, in turn, mediate calcium entry from the extracellular environment into the cytosol. Cytosolic Ca^{2+} is reversibly buffered by proteins and extruded back from the cell.

EXTRACELLULAR VEGF EVOLUTION. The evolution of the exogenous VEGF constitutes the extracellular environment the cell responds to with its surface tyrosine kinase receptors. The VEGF spatial profile satisfies the following diffusion equation:

$$\frac{\partial V(\mathbf{x},t)}{\partial t} = D_V \nabla^2 V(\mathbf{x},t) - \lambda_V V(\mathbf{x},t) - B(\mathbf{x},t,V(\mathbf{x},t)) + S, \tag{2.12}$$

where $V(\mathbf{x},t)$ denotes the actual concentration of the peptide at medium site **x** (i.e., $\sigma(\mathbf{x}) = 0$). The coefficients of diffusivity, $D_V > 0$, and of degradation, λ_V, are assumed to be homogeneous throughout the extracellular environment and derived from previous experimental determinations [92]. S describes the production of VEGF at a constant rate ϕ_V per unit of time by a discrete source, whose location and extension will be discussed in the next section. B is the amount of VEGF molecules per unit of time that are locally sequestered by the cell. Following [6, 56], we assume that receptor binding occurs very rapidly compared to the time-scale of cell migration, and that the local quantity of VEGF molecules instantly bound by the vascular EC at time t is equal to the smallest between the actual available molecular concentration V and the actual maximal amount of VEGF that can be internalized by the cell surface receptors, which is defined with $\beta_V(t)$ (whose estimation is described in details in the Appendix). Thus we set:

$$B(\mathbf{x},t,V(\mathbf{x},t)) = \min\{\beta_V(t), vV(\mathbf{x},t)\}, \tag{2.13}$$

where **x** belongs to the external surface of the cell PM (i.e., $\sigma(\mathbf{x}) = 0$ and σ(neighbor of **x**) $= 2$).

TABLE II - PARAMETERS INVOLVED IN THE MODEL

PARAMETER	DESCRIPTION	MODEL VALUE	REFERENCE
D_V	diffusion constant of VEGF	10 [μm^{2}s^{-1}]	[92]
λ_V	on-rate constant of VEGF degradation	$1.8 \cdot 10^{-4}$ [s^{-1}]	[92]
ϕ_V	on-rate constant of VEGF secretion	0.78 [h^{-1}]	[90, 92]
v	coefficient of the amount of bound VEGF per unit of time	1 [h^{-1}]	

INTRACELLULAR VEGF-INDUCED PATHWAYS. For the construction of a mathematical model of VEGF-mediated intracellular events, we use a PDE-type approach based on the model of L. Munaron for the proangiogenic calcium signals in a static EC [75]. However, with respect to that model, we here explicitly describe the VEGF-induced production of second messengers AA and NO, as well as the calcium feedback mechanism for AA biosynthesis. Moreover, we use slightly different flux distributions for both calcium entry and extrusion (see below for details).

The current levels of AA and NO at cell location **x** ($\sigma(\mathbf{x}) \in \{1,2\}$) are controlled by standard reaction-diffusion equations consisting in terms for their production, diffusion within the cytosol, and natural decay:

$$\frac{\partial AA(\mathbf{x},t)}{\partial t} = D_{AA} \nabla^2 AA(\mathbf{x},t) - \lambda_{AA} AA(\mathbf{x},t) + \frac{k_{AA} R(\mathbf{x},t)}{K_{AA} + R(\mathbf{x},t)} + \frac{v_{Ca} Ca(\mathbf{x},t)}{c_{AA} + Ca(\mathbf{x},t)}; \tag{2.14}$$

$$\frac{\partial NO(\mathbf{x},t)}{\partial t} = D_{NO}\nabla^2 NO(\mathbf{x},t) - \lambda_{NO} NO(\mathbf{x},t) + \frac{k_{NO} R(\mathbf{x},t)}{K_{NO} + R(\mathbf{x},t)} + v_{CaAA} \frac{Ca(\mathbf{x},t)}{c_{NO} + Ca(\mathbf{x},t)} \frac{AA(\mathbf{x},t)}{a_{AA} + AA(\mathbf{x},t)}. \tag{2.15}$$

The coefficients of diffusivity, D_{AA}, $D_{NO} > 0$, are assumed to be homogeneous within the cells. The degradation of both the intracellular messengers (and thus the following production of, respectively, eicosanoids [44] and peroxynitrites [79]) is also considered constant, at rates λ_{AA}, $\lambda_{NO} > 0$. The third terms in Eq. (2.14) and (2.15) describe the VEGF-induced production rate of AA and NO at the cell sub membrane region, as

$$R(\mathbf{x},t) = \sum_{\mathbf{x}'} B(\mathbf{x}',t), \tag{2.16}$$

where $B(\mathbf{x}',t)$ is defined as in (2.13) and, in particular, the $\mathbf{x}'$s form the extracellular first-nearest neighborhood of the cytosolic site $\mathbf{x}$ (i.e., $\sigma(\mathbf{x}) = 2$ and $\sigma(\mathbf{x}') = 0$). We apply a Michaelis-Menten law supposing that the intermediate receptor-ligand complexes are in a pseudo-steady state. Note that in this single simplified reaction, we bundle multiple signal transduction cascades, that are known intermediates in AA and NO generation, such as the activity of PLA2 and eNOS enzymes. The last term in Eq. (2.14) implements the calcium-dependent feedback mechanism in AA biosynthesis, while the analogous term in Eq. (2.15) accounts for the double regulation of NO production (both AA- and Ca^{2+}-mediated). They are described by others saturating functions of the Michaelis-Menten type, work within the entire cell cytosol and agree with electrophysiological measurements, see again [75].

The intracellular level of calcium at site $\mathbf{x}$ ($\sigma(\mathbf{x}) \in \{1,2\}$), defined $Ca(\mathbf{x},t)$, is determined by a balance between the influxes through either AA- and NO-activated PM channels, respectively F_{AA} and F_{NO}, extrusion of the ion from the cytosol, F_{out}, and its buffering. It is thus controlled by the following reaction-diffusion equation:

$$\frac{\partial Ca(\mathbf{x},t)}{\partial t} = K_{buff}\left[D_{Ca}\nabla^2 Ca(\mathbf{x},t) + F_{AA}(t) + F_{NO}(t) - F_{out}(t)\right]. \tag{2.17}$$

The coefficient of diffusion, $D_{Ca} > 0$, is assumed to be homogeneous throughout the cell (the diffusion of calcium across the nuclear envelope is taken to occur through non selective pores, whose permeability is proportional to the diffusion constant of the ion in the cytosol [21, 75]). F_{out}, the overall rate of calcium efflux from the cell at time t, incorporates the extrusion of the ion both via PM ATP-ase and Ca^{2+}-Na^{2+} exchangers, which is given in several models as a sum of Hill functions [75, 100]. However, in order to avoid over-complications while remaining close to the curves set in literature in the considered agonist concentration range, we here approximate F_{out} as a single Michaelis-Menten form:

$$F_{out}(t) = \sum_{\partial\mathbf{x}-membrane} F_{out}(\partial\mathbf{x},t) = \sum_{\partial\mathbf{x}-membrane} k_{Ca}\left[\frac{Ca(\mathbf{x},t)}{Ca_{out}+Ca(\mathbf{x},t)}\right], \tag{2.18}$$

where $\partial\mathbf{x}$ is the external border of cell membrane site $\mathbf{x}$ (as usual, $\sigma(\mathbf{x}) = 0$ and $\sigma(\text{neighbor of } \mathbf{x}) = 2$), k_{Ca} is the maximal rate of calcium extrusion and Ca_{out} the calcium concentration at which the rate of efflux is half maximal. F_{AA} and F_{NO}, respectively the Ca^{2+} influx distributions from the extracellular environment through independent and either AA- and NO-activated channels, are assumed to be saturably dependent on the relative second messenger concentration:

$$F_{AA}(t) = \sum_{\partial\mathbf{x}-membrane} F_{AA}(\partial\mathbf{x},t) = \sum_{\partial\mathbf{x}-membrane} F_{AA,max}\left[\frac{AA(\mathbf{x},t)}{q_{AA}+AA(\mathbf{x},t)}\right]^2 \tag{2.19}$$

$$F_{NO}(t) = \sum_{\partial\mathbf{x}-membrane} F_{NO}(\partial\mathbf{x},t) = \sum_{\partial\mathbf{x}-membrane} F_{NO,max}\left[\frac{NO(\mathbf{x},t)}{q_{NO}+NO(\mathbf{x},t)}\right]^2, \tag{2.20}$$

where $\partial\mathbf{x}$ is defined as in Eq. (2.18). The quadratic exponent reflects the fact that two AA or NO molecules are supposed to be bound to the respective Ca^{2+} channel in order to open it. There would be two additional fluxes that influence the level of cytosolic calcium: the rate of its release from the ER and the rate of its resequestration back in the endoplasmic reticulum [2, 86]. We can neglect both contributions, since the former is not stimulated by low concentrations of AA and NO [27, 67, 98], and the latter is typically involved only in the recovery of calcium response after agonist removal [66].

The scaling factor $K_{buff} = \frac{K_{off}}{K_{off}+K_{on}b_T}$ models the activity of intracellular endogenous buffers (proteins including calmodulin and others, cytoskeleton, mitochondria), which have a significant impact on the overall calcium dynamics, influencing its effective diffusion and contributing to decrease its level [8, 10, 46]. b_T is the total concentration of buffer sites (considered constant and experimentally estimated in different cell types), K_{on} is the rate of calcium uptake, K_{off} the rate of its release. This approximation works under the assumption that the buffering reactions take place on a faster timescale than the flux dynamics described above, and thus they can be considered in a quasi-steady state. This is the case of immobile buffers, characterized by low affinity and fast kinetics [93, 94].

Finally, the extracellular level of calcium evolves according to:

$$\frac{\partial Ca_{ext}(\mathbf{x},t)}{\partial t} = D_{Ca}\nabla^2 Ca_{ext}(\mathbf{x},t) - F_{AA}(t) - F_{NO}(t) + F_{out}(t). \tag{2.21}$$

where $\sigma(\mathbf{x}) = 0$, and the fluxes F_{AA}, F_{NO}, and F_{out} are characterized in Eqs. (2.18), (2.19), and (2.20).

TABLE I - PARAMETERS INVOLVED IN THE MODEL

PARAMETER	DESCRIPTION	MODEL VALUE	REFERENCE
D_{AA}	diffusion constant of AA	10 [$\mu m^2 s^{-1}$]	[75]
λ_{AA}	on-rate constant of AA degradation	30 [s^{-1}]	[75]
k_{AA}	maximal rate of VEGF-dependent AA release	30 [$\mu M s^{-1}$]	fit to experiments in [75]
K_{AA}	Michaelis-Menten constant for VEGF-dependent AA release	1 [μM]	fit to experiments in [75]
v_{Ca}	maximal rate of Ca-dependent AA release	0.75 [$\mu M s^{-1}$]	
c_{AA}	Michaelis-Menten constant for Ca-dependent NO release	0.3 [μM]	
D_{NO}	diffusion constant of NO	3300 [$\mu m^2 s^{-1}$]	[52, 75]
λ_{NO}	on-rate constant of NO degradation	0.1 [s^{-1}]	[75]
k_{NO}	maximal rate of VEGF-dependent NO release	30 [$\mu M s^{-1}$]	
K_{NO}	Michaelis-Menten constant for VEGF-dependent NO release	1 [μM]	
v_{CaAA}	maximal rate of NO release	1.5 [$\mu M s^{-1}$]	fit to experiments in [14, 67]
c_{NO}	dissociation constant between Ca and eNOS	0.3 [μM]	[83]
a_{AA}	dissociation constant between AA and eNOS	0.2 [μM]	[75]
Ca_0	local intracellular basal calcium level	0.05 [μM]	[10, 75]
$Ca_{ext,0}$	extracellular calcium level	2000 [μM]	[10, 75]
D_{Ca}	diffusion constant of Ca	220 [$\mu m^2 s^{-1}$]	[26, 46, 75]
k_{Ca}	maximal rate of calcium efflux	24.7 [$\mu M s^{-1}$]	fit to models in [75, 100]
Ca_{out}	threshold concentration for calcium extrusion	0.32 [μM]	fit to models in [75, 100]
$F_{AA,max}$	maximal rate of calcium influx through AA-activated channels	6 [s^{-1}]	fit to experiments in [67, 75]
$F_{NO,max}$	maximal rate of calcium influx through NO-activated channels	4.5 [s^{-1}]	fit to experiments in [67, 75]
q_{AA}	Michaelis-Menten constant for AA-activated channels	2 [μM]	fit to experiments in [67, 75]
q_{NO}	Michaelis-Menten constant for NO-activated channels	5 [μM]	fit to experiments in [67, 75]
K_{off}	dissociation constant between endogenous buffers and Ca_c	300 [s^{-1}]	[8]
K_{on}	on-rate constant of endogenous Ca_c buffering	100 [$\mu M^{-1} s^{-1}$]	[8]
b_T	total endogenous buffer concentration	450 [μM]	[26, 75]

3 Simulations and Results

Numerical simulations of the model framework are run with a modified and adapted version of the open-source Compucell3D[2] environment [34, 84]. We have in fact implemented tools for a computationally efficient integration of the different biological scales spanned by our approach: in particular, subroutines and plug-ins are set to inherit, at each time step, the biophysical properties of the EC from its microscopic biochemical state[3].

The simulated domain consists in a 600 $\times$ 200 $\times$ 80 square lattice with periodic boundary conditions. One lattice voxel is equivalent to 0.125 μm^3: thus the lattice represents a 300 μm $\times$ 100 μm $\times$ 40 μm *motility chamber* with a volume of 1.2 $\cdot$ 10^6 μm^3. One Monte Carlo Step corresponds to 10 s. The PDEs are numerically solved using a finite-difference (FD) scheme on grids with the same spatial resolution of the CPM lattice, and with 10 diffusion timesteps per MCS. Such timesteps are sufficiently small to guarantee numerical stability.

The hemispheric vascular EC, whose initial measures are given in Table I, is placed in the right side of the simulation environment. The biological variables are initiated at their typical levels: in particular, there are no AA and NO within the cell, and the free cytosolic calcium, Ca_0, is assumed uniform, as well as the extracellular level of the ion, $Ca_{ext,0}$. All the parameters involved in the model are listed in Tables I, II, and III.

We run a first set of simulation in *control conditions*, i.e. without the application of external chemical stimuli. As expected, no calcium events take place ($Ca(t = 6$ h)=Ca_0), according to experimental observation made by Munaron for his model in [75], and we do not observe any spontaneous change in the shape of the EC, which remains more or less hemispheric and starts a slow isotropic motion, see Fig. 5. Such cell behavior is qualitatively consistent with *in vitro* experiments, where a block in VEGF signaling causes endothelial cells to keep a round shape [23] and to have a substantially negligible autonomous motility [81]. In particular, this last consideration gives us confidence to compare our model and with the experimental results therein also to quantitatively, in order to estimate the basal properties of the cell (see the Appendix for a detailed explanation).

A point source of VEGF (S in Eq. (2.17)) is then applied in **x**=(600, 100, 0). Figure 6 (and Video S1) shows time lapse images of both the phenomenological migration of the cell and the relative calcium events. As represented in Fig. 6(A), the motile cell undergoes a gradual transition from the initial symmetric stationary state to a polarized migratory state, characterized by clearly distinguishable leading and trailing edges. In particular, a long and thin membrane-bound cytoplasmic pseudopodium emerges at the front of the cell, defining the direction of migration toward the chemotactic source, as the elongated cell moves by constantly protruding at the leading edge, while retracting

[2] downloadable at http://www.compucell3d.org

[3] In the free-ware spirit of CompuCell3D, the interested readers may contact the author to get further clarifications on the model implementation and, eventually, to get the relative subroutines and plug-ins

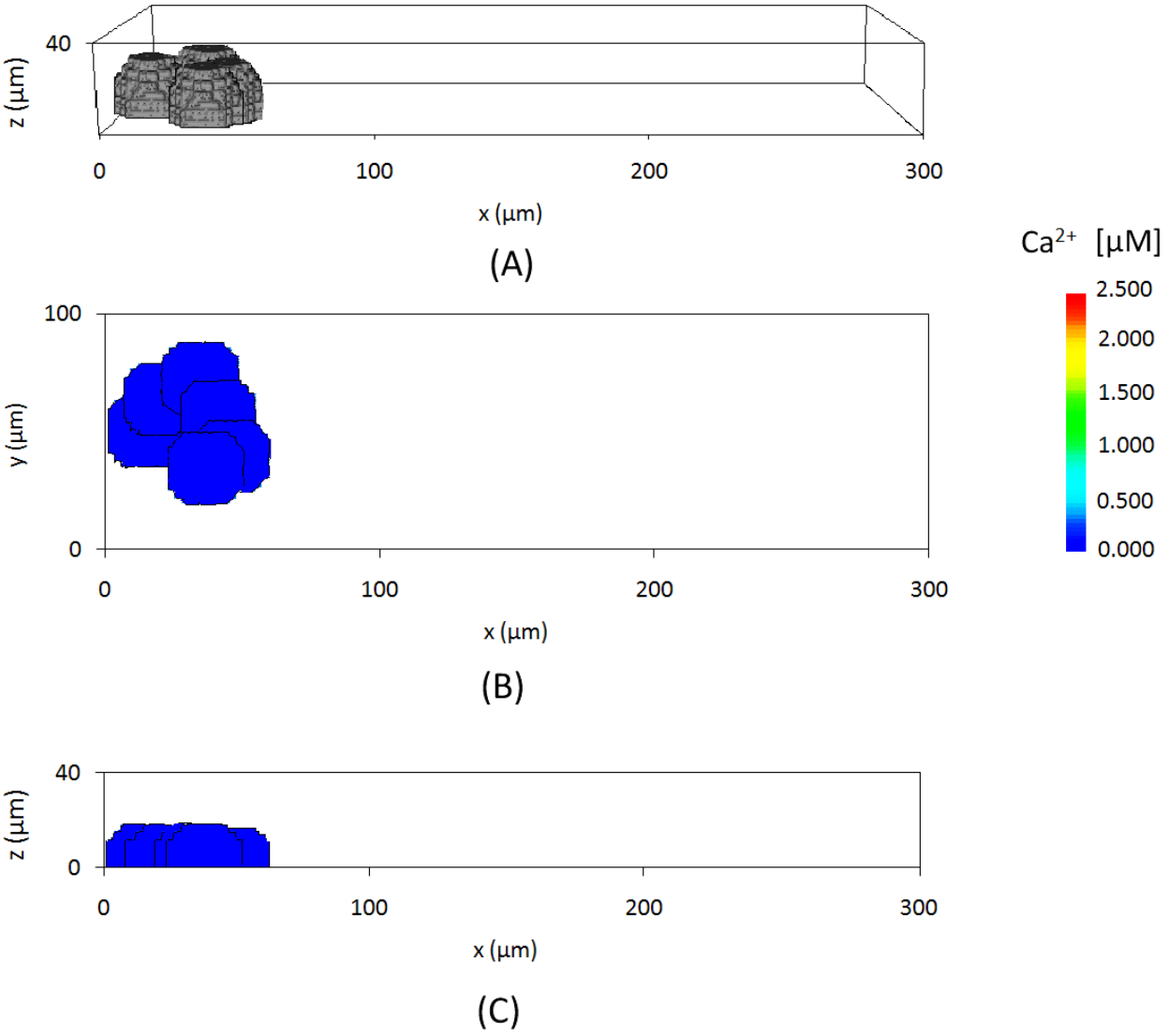

Figure 5: Endothelial cell phenomenology and relative calcium events in *control conditions* (without external stimuli) at 30 min intervals until $t = 3$ h. (A) Three-dimensional view of cell migration. Contour plot showing cell position and intracellular calcium concentration in (B) z=1 μm plane and (C) y=50 μm plane. Calcium concentration has been pseudocolor-scaled so that the maximum value is red. The simulated cell almost maintains its initial hemispheric morphology and undergoes an essentially random motion. No calcium signals are observed.

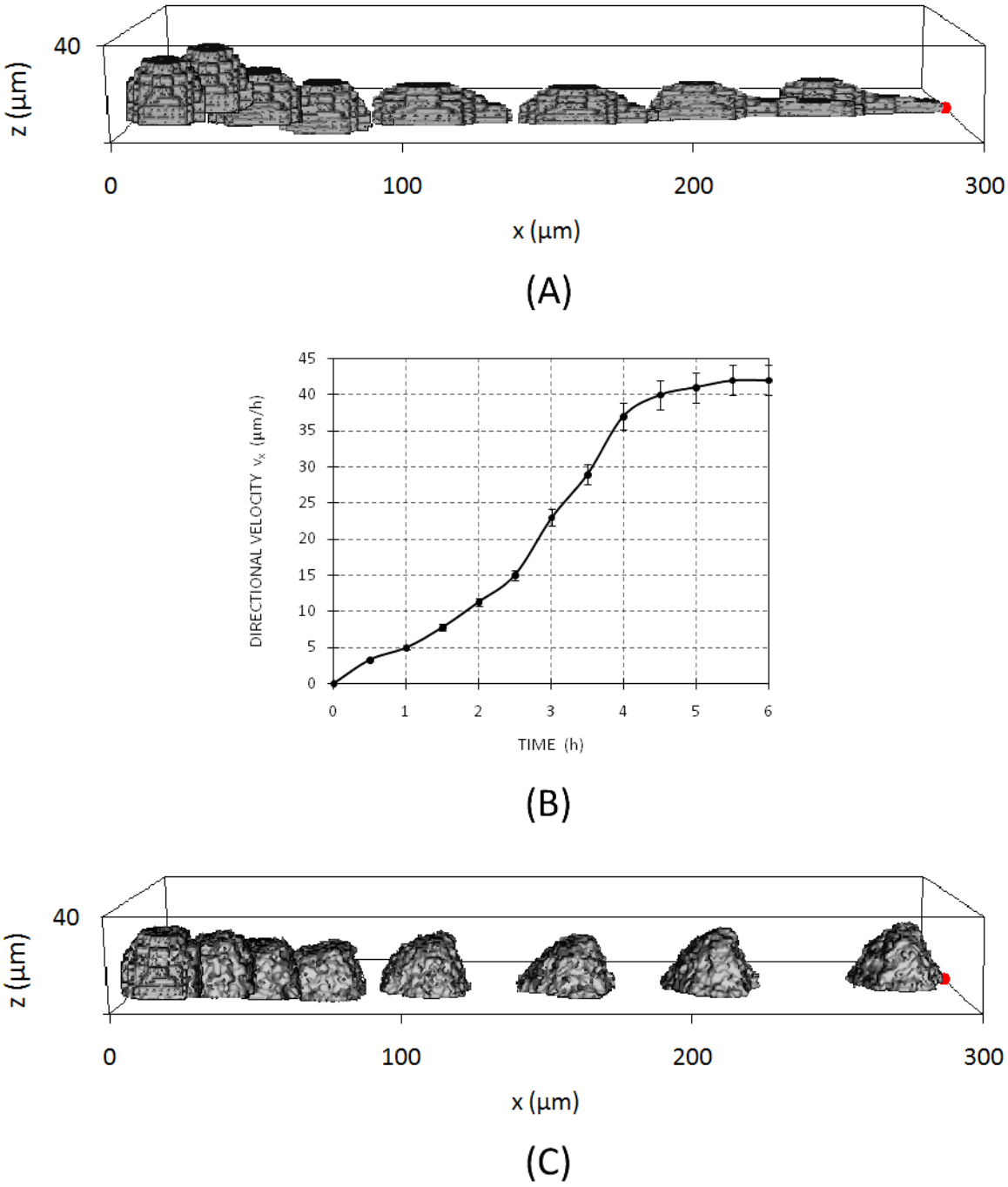

Figure 6: VEGF-induced chemotactic migration and cell polarization. (A) Representative three-dimensional views taken at 45 min intervals until $t = 6$ h. Red dot represents the VEGF source. The cell, after a short latency, rapidly polarizes establishing a leading edge, a long and thin pseudopodium, which gives the direction of motion. (B) Cell directional velocity (i.e. toward the chemotactic source) $v_x = (x_{CM}(t + \Delta t) - x_{CM}(t - \Delta t))/2\Delta t$, where the x_{CM} is the x-coordinate of the cell center of mass and $\Delta t = 10$ min [81]. Mean over 10 simulations, error bars represent standard deviation. (C) For comparison purposes, model results in the case of a monocompartmental endothelial cell (i.e., formed by a unique unit representing an undifferentiated cytoplasm). All the other parameters are the same as the previous case. It is worth to notice that this approach is unable to reproduce cell polarization, as the cell is only a deformed mass that moves toward the chemical source.

at the rear. Such a phenomenology is coherent with *in vitro* realizations performed in [23], where VEGF-stimulated ECs are found to assume an extended, bipolar morphology. In the presented model, cell elongation results from the interplay between the chemotactic-induced membrane extension at the leading front of the cell and the mechanical properties given to its compartments, with the nucleus characterized by a constant stiffness and the cytoplasm by variable calcium-dependent elasticity and motility. In particular, the exogenous stimulus causes the cell plasmamembrane to locally protrude in the direction of increasing VEGF gradients, with a speed of protrusion proportional to the modulus of the local chemical strength μ_{ch} itself (for instance, in any CPM model the simulated objects experience an implicit drag force from the lattice, and thus they have Aristotelian dynamics, refer to [4, 58] for more detailed comments). Pushed by the leading front, the overall cytosolic region, whose elasticity and mobility increase due to the concomitantly calcium accumulation, then deforms and moves forward, while pulling onto the nucleus with the same force. The nucleus (which, as a CPM object, also follows Aristotelian dynamics) is instead basically stuck to the underlying lattice, as a consequence of its rigidity: therefore it moves with a lower velocity than the surrounding cytosol and lags behind, creating the characteristic polarized morphology of the EC. These mechanisms are a simplified picture of the biological processes underlying cell movement (the relative literature is vast, however we refer the reader to the comprehensive biochemical reviews [82, 85] and the classical books [1, 39]). In reality, the external chemical stimulus, via surface receptors, triggers in fact the polymerization of the cell cytoskeleton, which results in the constant abutting of the cell plasmamembrane in the direction of motion and in the coordinated development and release of focal adhesions (FAs). During the motion of the overall cell, the nucleus is unable to have an autonomous directional movement, as it only negligibility fluctuates in the cytoplasmic fluid. However, the nucleus is anchored to intermediate actin filaments and microtubules, which are in turn linked to the extracellular matrix through the focal adhesion clusters: therefore, it is passively pulled by drag forces transmitted by the substrate via the cytoskeletal components, see review [104] and the references therein. Such indirect mechanical interactions between the nucleus and the matrix environment are implicitly reproduced by the model artifact of staking the nuclear compartment to the underlying lattice with a finite rigidity, which is sufficiently high to results in a slow movement of the nucleus but low enough to avoid the total block of its locomotion. Obviously, a more realistic model should explicitly include the dynamics of the cell cytoskeleton and its signal transduction (this topic, often approached in the literature with multiphase models, see for example the book [19], could represent a fundamental improvement of CPM applications, since it has received little though increasing attention). However, the assumption made does not strongly influence the final outcomes of the model: the dynamics of the nucleus are in fact kept constant in all the proposed sets of simulations by fixing the value of its stiffness, λ_1, and of its mobility, T_1: in this way, the migratory properties of the EC are mainly determined by the other mechanisms involved (such as molecular processes), which instead vary in each case. The

importance of the compartmentalized approach is also underlined by studying the phenomenology of the cell in the case of a monocompartmental representation (i.e., the EC is formed by a single, undifferentiated cytoplasm, while all the other model assumptions are not changed): as reproduced in Fig. 6(C), the polarization process does not emerge and the cell is a deformed mass which moves in the direction of the chemical source (notice that also the top of the cell unrealistically protrudes). For a quantitative characterization of cell motility, we define cell average *directional displacement* and *velocity* (i.e., along the x-axes, in the direction of the chemical source), which facilitate the comparison between the analyzed experimental conditions. In particular, the cell directional displacement is simply the x-coordinate of the cell center of mass, x_{CM}, at a given time, while the directional velocity is the relative component of its velocity (i.e., $v_x = (x_{CM}(t) - x_{CM}(t - \Delta t))/\Delta t$, where $\Delta t = 60$ MCS, and thus ≈ 10 min, as in Eq. (2.10)). After an initial stage, when the cell is still round and does not strongly sense the VEGF stimulus, the directional velocity rapidly increases until it stabilizes at 42 μm/h (when the EC is completely polarized), see Fig. 6(B). This agrees with the range of speeds measured in [81] for real endothelial cells in embryonic mouse allantoides, i.e. (25 μm/h ; 40 μm/h). In particular, the cell velocity has been therein evaluated relative to the motility of the surrounding environment in which the cells reside: the observed lower values can be partly explained by the fact that the experiments are performed in a more realistic, noisy environment, that reduces the persistence length of cell motion. Moreover, the cell takes ≈ 6 hours to reach the opposite side of the chamber. In this case, obviously, $x_{CM}(t = 6 \text{ h})$ = 300 μm: this value is used as a reference value.

Figure 7 illustrates the time course of the intracellular calcium signals in two perpendicular sections of the cell. As reference sections we choose the z=2 vx (≈ 1 μm) plane, which includes the development of the pseudopodium, and the y=100 vx (≈ 50 μm) plane, the main transversal section of the cell. After a short latency ($\approx$ 30 min), surface receptor activation by VEGF stimulates the full activation of downstream cascade leading to the subsequent production of second messengers AA and NO, which, in turn, start to induce calcium influx from the extracellular environment through the relative channels. The resulting intracellular calcium events, initiating at the sub-plasma membrane regions, rapidly propagate in every direction, to inhomogeneously fill the whole cell volume. The final pattern of Ca^{2+} accumulation is strongly localized: higher concentrations (> 2 μM) occur in the leading front of the polarized cell (i.e., at the tip of the pseudopodium), and decay within a distance of 15-20 μm (< 1 μM). They are undetectable in the peri-nuclear regions (< 0.5 μM). Moreover, the rate of the final intracellular accumulation of the ion is $\widetilde{Ca}(t = 6 \text{ h}) \approx 3.6$. These findings are in agreement with both experimental [98] and modeling [75] data on the spatial propagation of calcium events in endothelial cells stimulated with angiogenic factors. If the external VEGF stimulus is subsequently removed, imposing $S = 0$, the production of AA and NO ceases and they rapidly decay. The cytosolic calcium, extruded by pumps and exchangers, then quickly returns to the baseline level Ca_0 (not shown).

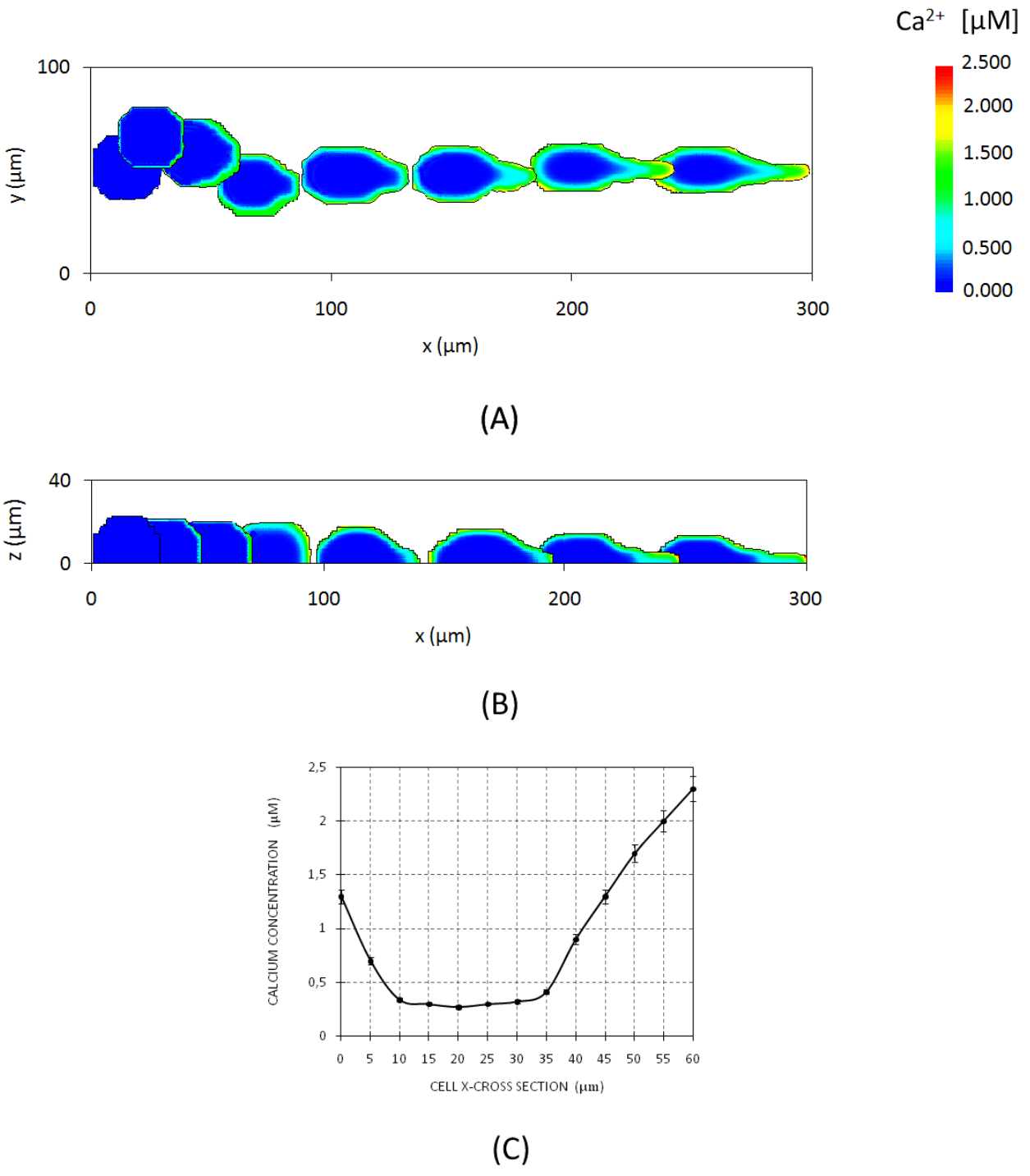

Figure 7: VEGF-induced calcium events. Contour plots showing intracellular calcium concentration during cell motion in (A) z=1 μm plane and (B) y=50 μm plane. Representative images taken at 45 min intervals until $t = 6$ h as in Fig. 6(A). (C) Ca^{2+} concentration profile at the end of migration, $t = 6$ h, along cell x-cross-section of z=1 μm plane from the trailing edge to the leading edge of the polarized cell. Mean over 10 simulations, error bars represent standard deviation. Higher Ca^{2+} accumulation (> 2 μM) is observed in the thin pseudopodium. Negligible calcium events are seen in the central-nuclear area (< 0.5 μM).

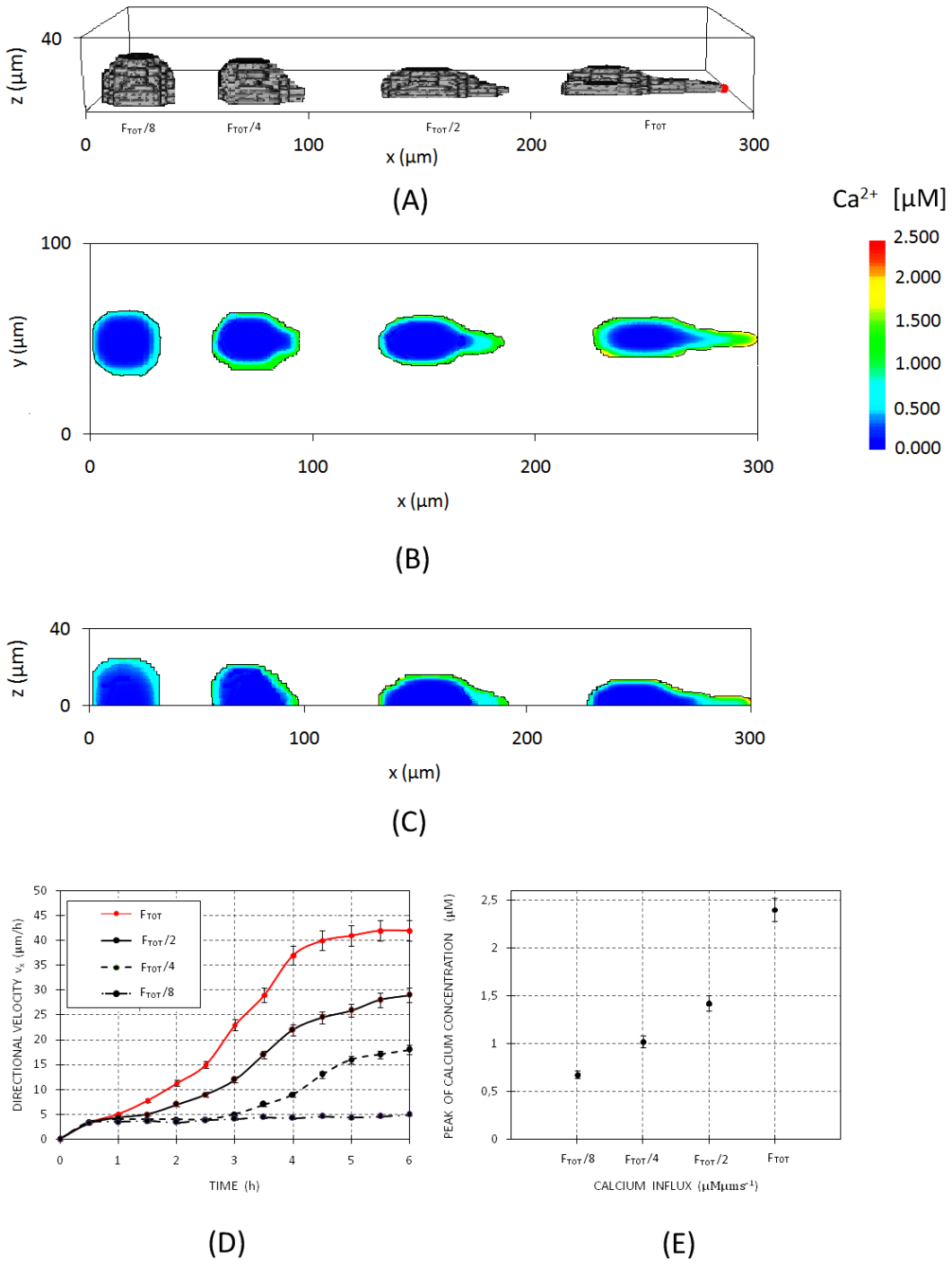

Figure 8: Partial inhibition of overall VEGF-induced calcium influx $F_{TOT} = F_{AA} + F_{NO}$. (A) Three-dimensional view of cell position at t=6 h for each F_{TOT}-decrement. Red dot represents the VEGF source. Contour plots showing the final intracellular calcium profile in (B) z=1 μm plane and (C) y=50 μm plane. Calcium concentration has been pseudocolor-scaled so that the maximum value is red. (D) Evolution in time of cell directional velocity v_x. The complete inhibition of calcium responses ($F_{TOT} = 0$) dramatically stops cell directional motility ($x_{CM}(t = 6\text{h}) = 20$ μm and $v_x \approx 3.3$ μm/h). (E) Maximal Ca^{2+} concentration at $t = 6$ h. Error bars show standard deviation over 10 simulations.

To establish a direct qualitative and quantitative relation between intracellular calcium events and cell motion, in Figure 8 we study the consequences of a gradual inhibition of the Ca^{2+} influx distributions. In particular, given that $F_{TOT} = F_{AA} + F_{NO}$ is the total VEGF-induced calcium influx, each of its decrement is the model counterpart of a treatment with an increasing concentration of carboxyamidotriazole (CAI) drug. CAI is in fact an anti-invasive and anti-angiogenic agent, which alters calcium-mediated signal transduction in ECs by blocking agonist-activated calcium entry in a dose-dependent manner [7, 47, 69]: in particular, it is currently under investigation as an orally administered tumoristatic agent in Phase II and III clinical trials for different tumors, as explained in [48, 76]. Decrements in F_{TOT} result in marked decrements in the cell directional velocity v_x, which are followed by the relative decrements in the final cell displacement ($x_{CM}(t = 6 \text{ h})$ = 150 μm for $F_{TOT}/2$ and $x_{CM}(t = 6 \text{ h})$ = 70 μm for $F_{TOT}/4$), see Fig. 8. Furthermore, an approximately complete inhibition of the mitogen-induced calcium responses, $F_{TOT} \longrightarrow 0$, causes the cell to remain in its unpolarized stationary state, dramatically stopping its directional locomotion, as for $F_{TOT}/8$, v_x is almost a constant ≈ 4 μm/h and $x_{CM}(t = 6 \text{ h}) < 20$ μm. The cell behavior is explained by the fact that partial inhibitions of F_{TOT} cause decrements in the intensity of calcium responses: in fact both the maximal peaks and the overall accumulation of the ion decrease (i.e., $\widetilde{Ca}(t = 6 \text{ h}) \approx 1.4$ for $F_{TOT}/2$, $\widetilde{Ca}(t = 6 \text{ h}) \approx 0.6$ for $F_{TOT}/4$, and $\widetilde{Ca}(t = 6 \text{ h}) \approx 0.2$ for $F_{TOT}/8$), see Fig. 8(E). The consequence is a downregulation of the biophysical properties of the EC, such as the intrinsic motility, elasticity and chemotactic strength, involved in its migratory capacity. However, the interferences in the influx distributions do not affect the spatial propagation of the ion, as represented in Fig. 8(B-C).

Disruptions in the second messenger machinery are as well of high biological interest. In particular, we exclude the production of arachidonic acid (similarly nitric oxide) by imposing $k_{AA} = v_{Ca} = 0$ in Eq. (2.14) (similarly $k_{NO} = v_{CaAA} = 0$ in Eq. (2.15)). It is the model counterpart of the activity of PLA2 (eNOS) inhibitor (such as AACOCF3 or, respectively, L-NAME drugs, which are well studied anti-angiogenic compounds both *in vitro* and *in vivo*, see again the excellent medical review [76]). Both exclusions result in an incomplete transition of the EC toward the motile phenotype, and in the consequent decrement of its directional velocity and final displacement ($x_{CM}(t = 6$ h) = 110 μm in the case of AA inhibition, and $x_{CM}(t = 6 \text{ h})$ = 180 μm in the case of NO inhibition), as shown in Fig. 9(A-D). The explanation is that the disruption in the biosynthesis of each of the two molecules extinguishes its intracellular presence and, consequently, abolishes the relative calcium influx, as also provided by the experimental system in [67]. Indeed, the final outcome of both proposed treatments is a downregulation of the VEGF-induced calcium signals similar to those obtained from the direct block of the influxes of the ion (reproduced in Fig. 8) which, as seen, have caused partial inhibitions of the cell migratory capacity. In particular, also with the exclusion of either AA or NO production, the spatial propagation of calcium responses appears relatively unchanged w.r.t. the standard

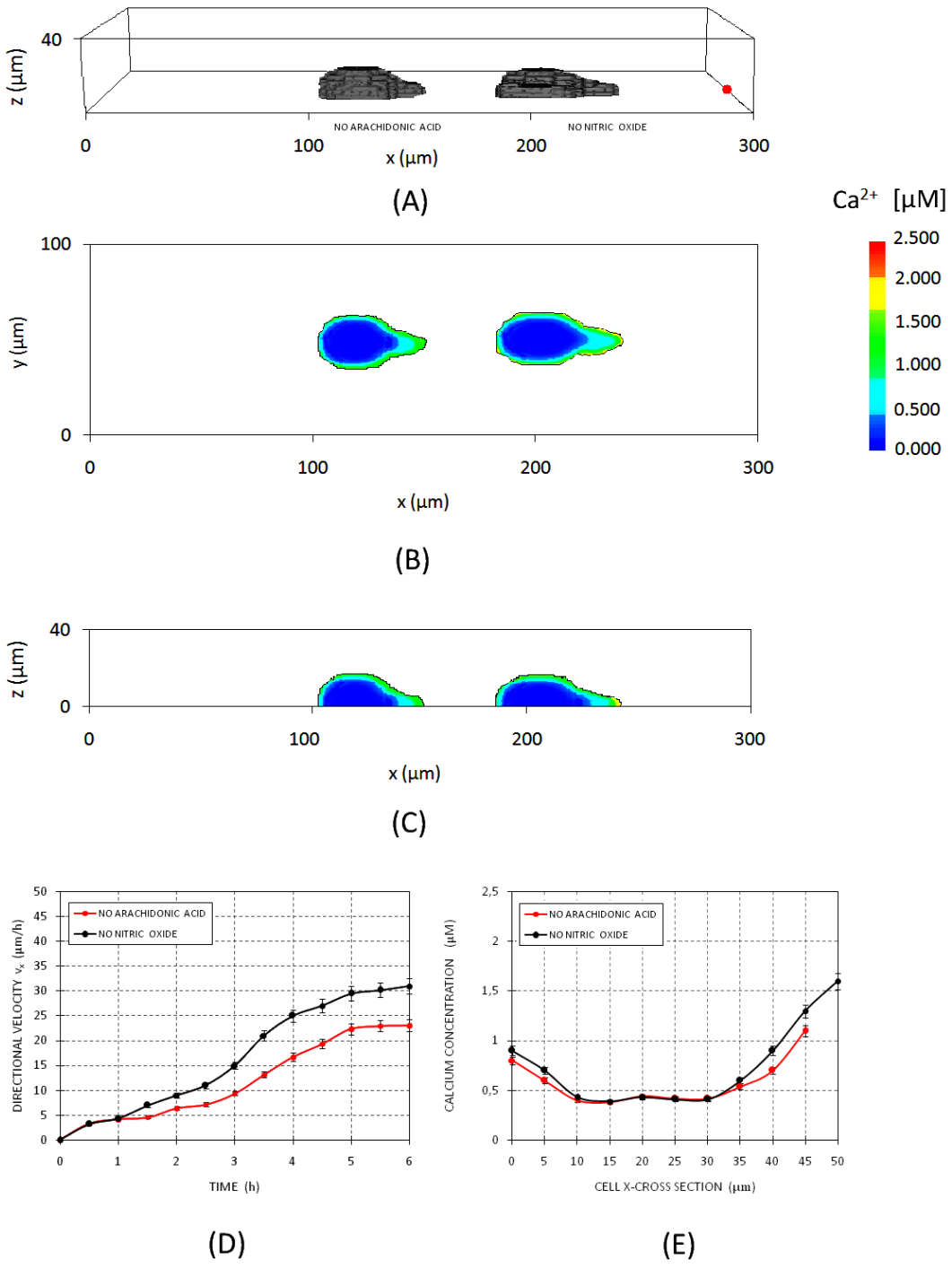

Figure 9: Modeling interference in the production of either arachidonic acid ($k_{AA} = v_{Ca} = 0$) and nitric oxide ($k_{NO} = v_{CaAA} = 0$). (A) Three-dimensional view of cell position at t=6 h for the two cases. Red dot represents the VEGF source. Contour plots showing the final intracellular calcium profile in (B) z=1 μm plane and (C) y=50 μm plane. Calcium concentration has been pseudocolor-scaled so that the maximum value is red. (D) Evolution in time of cell directional velocity v_x. (E) Ca^{2+} concentration profiles at the end of migration, $t = 6$ h, along cell x-cross-section of the z=1 μm plane from the trailing edge to the leading edge of the polarized cell. As usually, higher Ca^{2+} accumulations is observed in the thin pseudopodium, even if the maximal amplitudes are strongly decreased. Negligible calcium events are seen in the central-nuclear area (< 0.5 μM). Mean over 10 simulations, error bars represent standard deviation.

parameter setting, while the peaks have a lower amplitude (i.e., $\approx$ 1.1 μM in the case of AA inhibition and $\approx$ 1.6 μM in the case of NO inhibition) and the total intracellular amount a significative decrement as well (i.e., $\widetilde{Ca}(t = 6$ h)$\approx$ 1.2 in the case of AA inhibition and $\widetilde{Ca}(t = 6$ h) $\approx$ 1.6 in the case of NO inhibition), see Fig. 9(B-C-E). Taken together the results in Figs. 8 and 9, we have the model confirmation of the efficacy of two families of anti-angiogenic compounds, that target different calcium-dependent mechanisms involved in cell migration (i.e., either directly the fluxes through PM channels or the dynamics of the second messengers).

So far, we have provided the fact that differently modulated calcium signals influence the final morphology of the EC and its migratory properties. We now turn to the opposite by analyzing how a constrained cell shape affects cell migration, and the relative calcium events. We thus perform simulations forcing the vascular cell to keep its initial hemispheric morphology, with a high constant value of $\lambda_2 = 50$ in Eq. (2.4). This is the model counterpart of the activity of phalloidin-like compounds, which block the calcium-dependent reorganization of actin cytoskeleton by inhibiting actin-myosin interactions. As shown in Fig. 10 and in Video S2, the simulated endothelial cell, loosing its capacity to differentiate and polarize, is characterized by a shortly persistent motion, with a predominant random component, which results in a low directional velocity v_x and a short final displacement, as $x_{CM}(t = 6$ h) = 85 μm. These observations agrees well with the experimental results provided in [41], where more rounded and symmetric ECs are seen to have an isotropic migration, and suggest a possible pharmacological way to reduce cell motility. The constrained cell morphology affects also the pattern of calcium accumulation, see Fig. 10(E): the peaks remain localized in the sub-plasma membrane region of leading front of the cell (and almost negligible, $\ll 1$ μM, within a distance of 5-10 μm from the cell surface), but they occur slightly later, and have a significantly lower amplitude ($\approx$ 1.6 μM), as resulted also experimentally in [98] and theoretically in [75, 38]. Consistently, the overall accumulation of the ion is significantly decreased, as $\widetilde{Ca}(t = 6$ h) $\approx$ 1.1. These observations could provide an additional explanation of the great heterogeneity of calcium responses in the same population: not only calcium machinery expression can vary from cell to cell, but also in cells expressing the same amount of channels the response could significantly change in function of the their geometry. Moreover, with another view point, the same cell can vary its response to the same external chemical stimuli only by varying its shape, which is of particular relevance during vascular development, when the ECs constantly remodel.

When the external chemical signal is extended to the whole right lower edge of the migration chamber, with the same intensity ϕ_V, we observe a different cell shape reorganization, see Fig. 11(A) and Video S3. After an initial stage ($\approx$ 1 h), in which its phenomenology resembles the standard case in Fig. 6, the motile EC adapts to the new VEGF profile, featuring a flat and thin ($\approx$ 2 μm) lamella in the direction of motion. An interesting consideration that emerges here is that such a different morphological transition is completely self-generating, and only due to the new

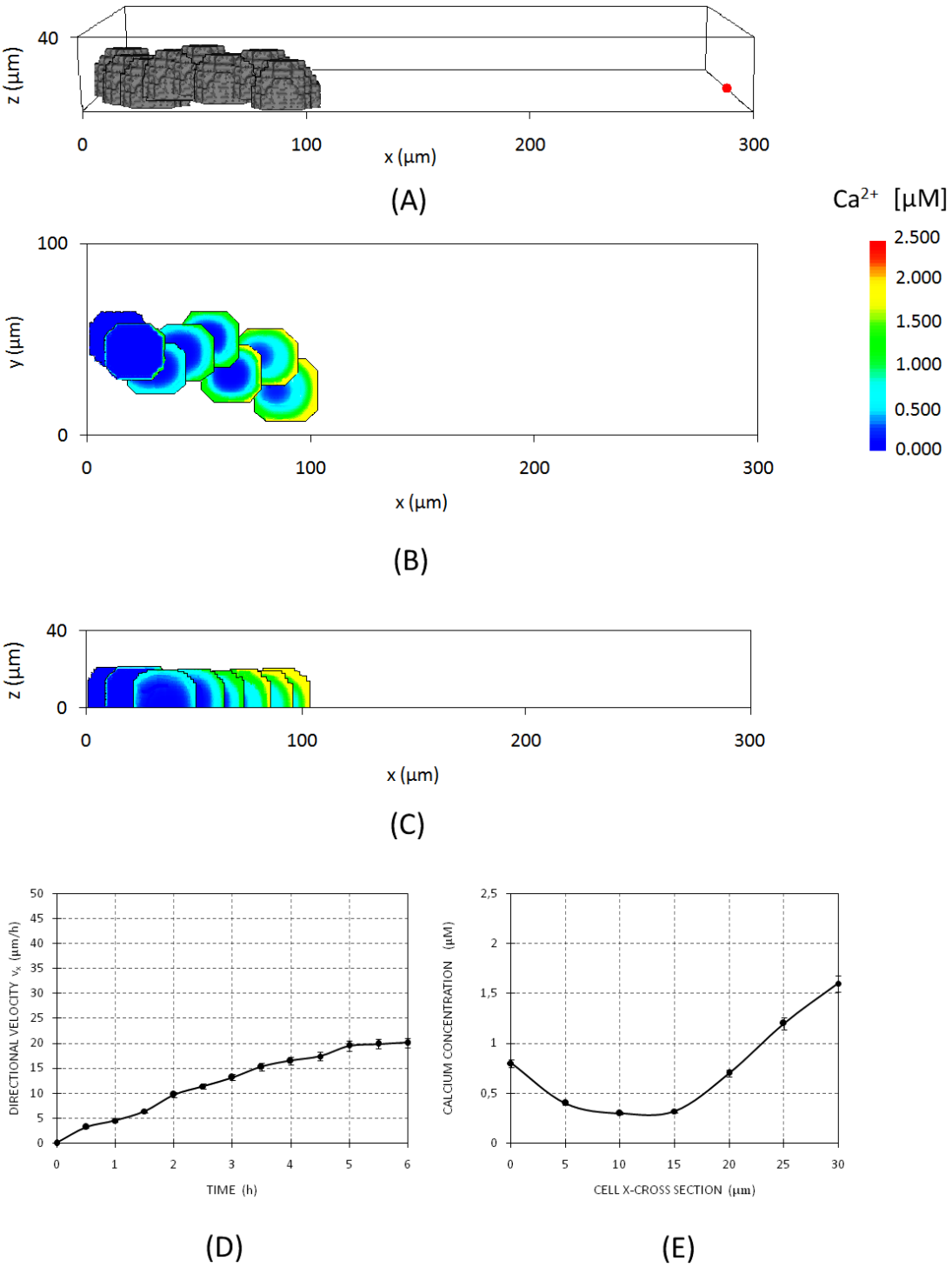

Figure 10: Inhibition of active cytoskeletal reorganization, $\lambda_2 = 50$. (A) Three-dimensional view of cell position (red dot represents the VEGF source), (B) and (C) contour plots showing intracellular calcium concentration during cell motion in, respectively, z=1 μm plane and y=50 μm plane. For (A), (B), and (C) representative images taken, as usually, at 45 min intervals until $t = 6$. (D) Evolution in time of cell directional velocity v_x. (E) Ca^{2+} concentration profiles at the end of migration, $t = 6$ h, along cell x-cross-section of the z=1 μm plane from the trailing edge to the leading edge. Mean over 10 simulations, error bars represent standard deviation.

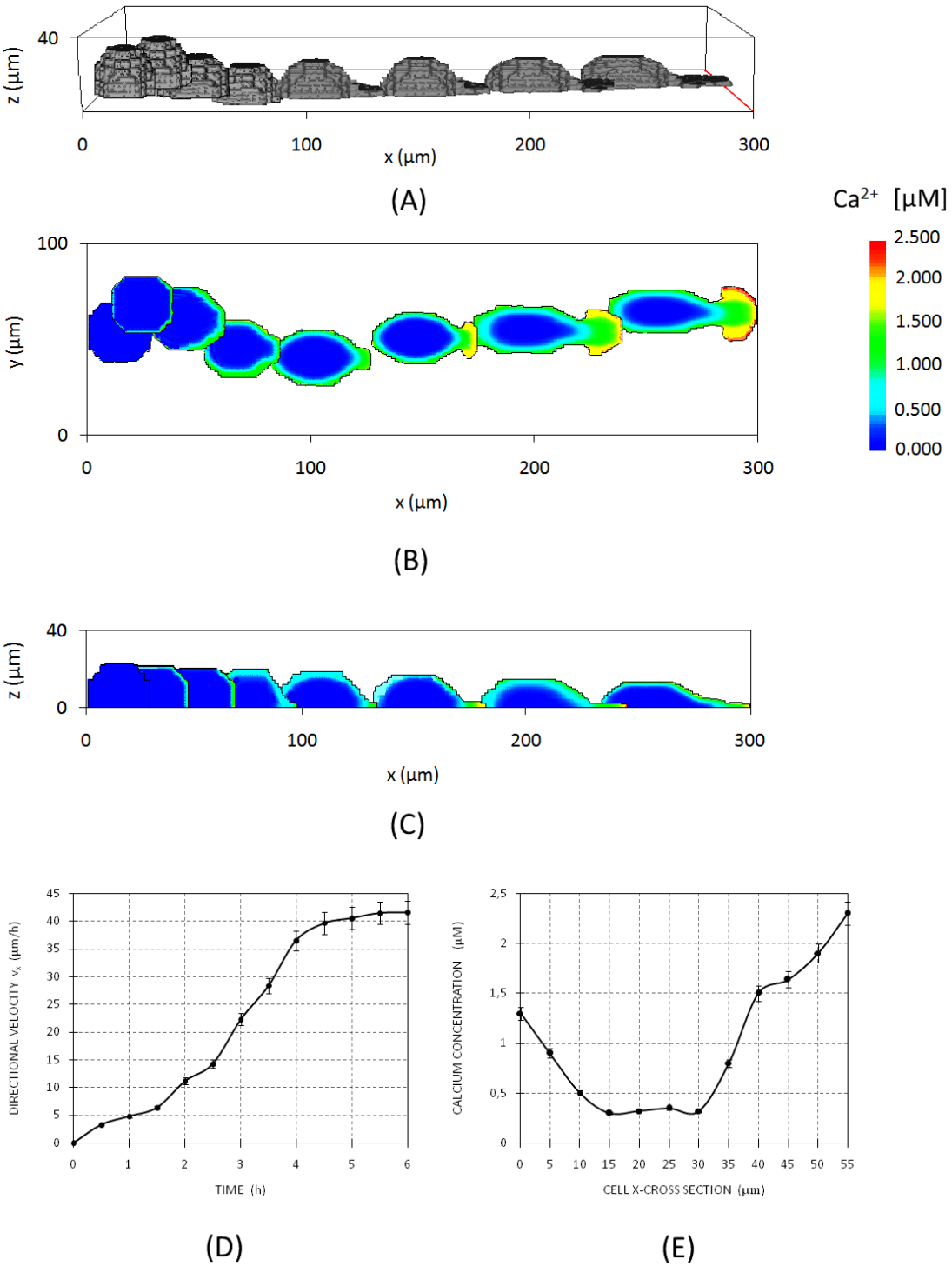

Figure 11: VEGF source extended to the whole right lower edge of the migration chamber. (A) Three-dimensional view of cell position (red line represents the VEGF source), (B) and (C) contour plots showing intracellular calcium concentration during cell motion in, respectively, z=1 μm plane and y=50 μm plane. For (A), (B), and (C) representative images taken, as usually, at 45 min intervals until $t = 6$. (D) Evolution in time of cell directional velocity v_x. (E) Ca^{2+} concentration profiles at the end of migration, $t = 6$ h, along cell x-cross-section of the z=1 μm plane from the trailing edge to the leading edge. Mean over 10 simulations, error bars represent standard deviation.

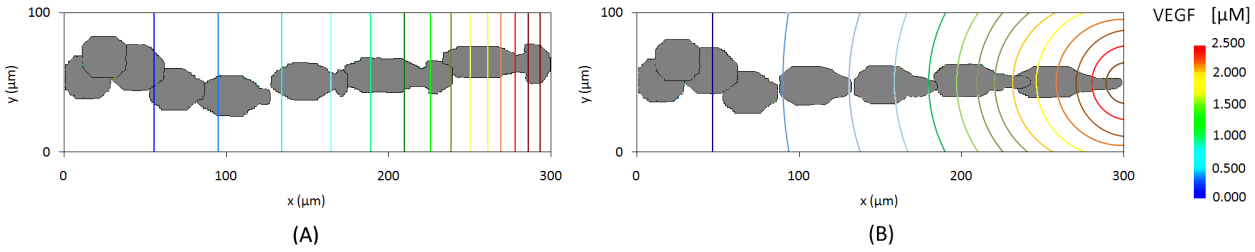

Figure 12: Cell morphological transition in the case of (A) planar (B) punctual VEGF source. Representation of the z=1 μm plane. Colored isolines indicate chemical levels.

spatial profile of the external stimulus as, beside the extension of the VEGF source, we have not changed any other model assumptions. The mechanical explanation is that, as reproduced in Fig. 12(A), the planar chemical source results in a planar front of maximal concentration, which chemotactitally stimulates a larger part of the cell membrane to protrude, thus forming the flat lamella. On the opposite, the standard VEGF point source features a curved profile: consequently, the maximal chemical force, given by the maximal chemical gradient, is concentrated on a restricted part of the cell leading surface, from which the thin pseudopodium emerges, see Fig. 12(B). A further confirmation of this mechanism is given by the fact that, at the beginning of both simulations, when the curvature effects are not so strong, the morphology of the cell is very similar. As far as we know, there are no *in vitro* evidences replicating such a model outcome, probably because it is very difficult to experimentally vary the local spatial extension of a chemical source. However, this result is supported by plausible biomechanical implications. External chemical signals are in fact demonstrated to be locally transmitted from membrane-bound receptors to the nearest "central nodes" of cell cytoskeleton, including small G-proteins Cdc42, Rac and Rho [37, 31, 97]. The activity of the rho-family molecules, in turn, directly drives actin dynamics, regulating and fine-tuning polimerization and nucleation processes of cytoskeletal filaments, which determine the remodeling of the cytosol and the protrusion of the plasma-membrane [24, 59, 78]. An extended (i.e., not punctual) exogenous signal may therefore cause the growth of the actin filament network in a larger part of the cell leading front, eventually resulting in the formation of a flat motility structure, as the lamella emerged in our simulations. Interestingly, as shown in Fig. 11, the evolution of the cell migratory properties (the overall displacement, as $x_{CM}(t = 6 \text{ h})$ = 300 μm, and the directional velocity) remains almost unaltered w.r.t. the standard case as well as the VEGF-induced calcium dynamics. In particular, the peak of maximal calcium response, which remains localized in the thinner part of the cell (in the lamellipodium), measures ≈ 2.2 μM, while $\widetilde{Ca}(t = 6 \text{ h}) \approx 3.4$. This consideration provides the fact that proangiogenic Ca^{2+} signals are typically localized in the motility structures (either pseudopodia or lamellipodia) of vascular cells: such a peculiar pattern could in principle carry information of the specific role of the ion in other cellular functions, such as the adhesive interactions with neighboring cells during

the formation of vascular chords.

The model has been able to characterize the phenomenological migration of a VEGF-stimulated vascular cell and the relative calcium events, to reproduce the activity of some anti-angiogenic pharmacological compounds, and to suggest the use of already existing drugs (such as phalloidin-like compounds) to inhibit cell locomotion. We now can turn to perform simulations that provide additional insights of the calcium-dependent factors that control the migratory properties of the vascular cell. In particular, we focus on some conditions that would be difficult or impossible to actually establish *in vitro*, but that can suggest nonintuitive, but potentially very effective ways to interfere with the motility capacity of the EC.

The diffusion is clearly a crucial element in the intracellular propagation of calcium, and therefore affects a number of localized biochemical processes, as the feedback mechanism included in the kinetic scheme of AA and NO and the cell chemical sensitivity. A quantification of its importance is tested by setting D_{Ca}= 0 in Eq. (2.17). Without diffusion, the calcium ions entered from the medium are completely sequestered in the inner surface of the PM, and therefore calcium signals do not longer occur throughout the entire cell volume, see Fig. 13(B-C-E). In particular, the cell quickly reaches the peaks of calcium accumulation, which have the same intensity and localization (i.e., at the tip of the pseudopodium) as in the standard case. However, the EC undergoes only a partial elongation, which results in a lower directional velocity and a consequent decrement in the final displacement, as $x_{CM}(t = 6 \text{ h})$ = 165 μm, see Fig. 13(A-D). These results have a clear biological relevance, since they represent a definitive demonstration that the cell migratory properties are not established by the maximal amplitude of calcium responses (which, as seen, remains unchanged), but by the overall intracellular concentration of the ion, which is obviously strongly reduced by the exclusion of its diffusive behavior, as $\widetilde{Ca}(t = 6 \text{ h}) \approx 0.9$.

Modelling allows us to assess the perturbing effect of endogenous buffers on calcium signalling and on the overall migratory capacity of the cell. In the absence of buffers (i.e., by imposing $K_{buff} = 1$ in Eq. (2.17)), the spatial dynamics of Ca^{2+} events are not affected, but, as expected, the local concentrations are greater than control, see Fig. 13(B-C-H). In particular, the intracellular region in which calcium signals are not detectable decreases in size, as it is now restricted in the close proximity of the nucleus (at this regards, it is useful to compare the spatial profiles of the ion in Figs. 7 and 13). The consequent increment in the total intracellular calcium level (i.e., $\widetilde{Ca}(t = 5 \text{ h}) \approx 3.9$) enhances the migratory capacities of the EC, as the effective velocity grows up to $\approx$ 46 μ/h, and the cell reaches the opposite side of the chamber in nearly 5 hours, as shown in Fig. 14(A-G). We finally model a spatially inhomogeneous buffer distribution: in particular, an increasing clusterization of buffers is set toward the central regions of the cell, where the perinuclear mitochondria are more concentrated (as widely shown in literature [1] and confirmed by Munaron by staining with mitotracker [75]). Mathematically, we locally vary factor K_{buff}:

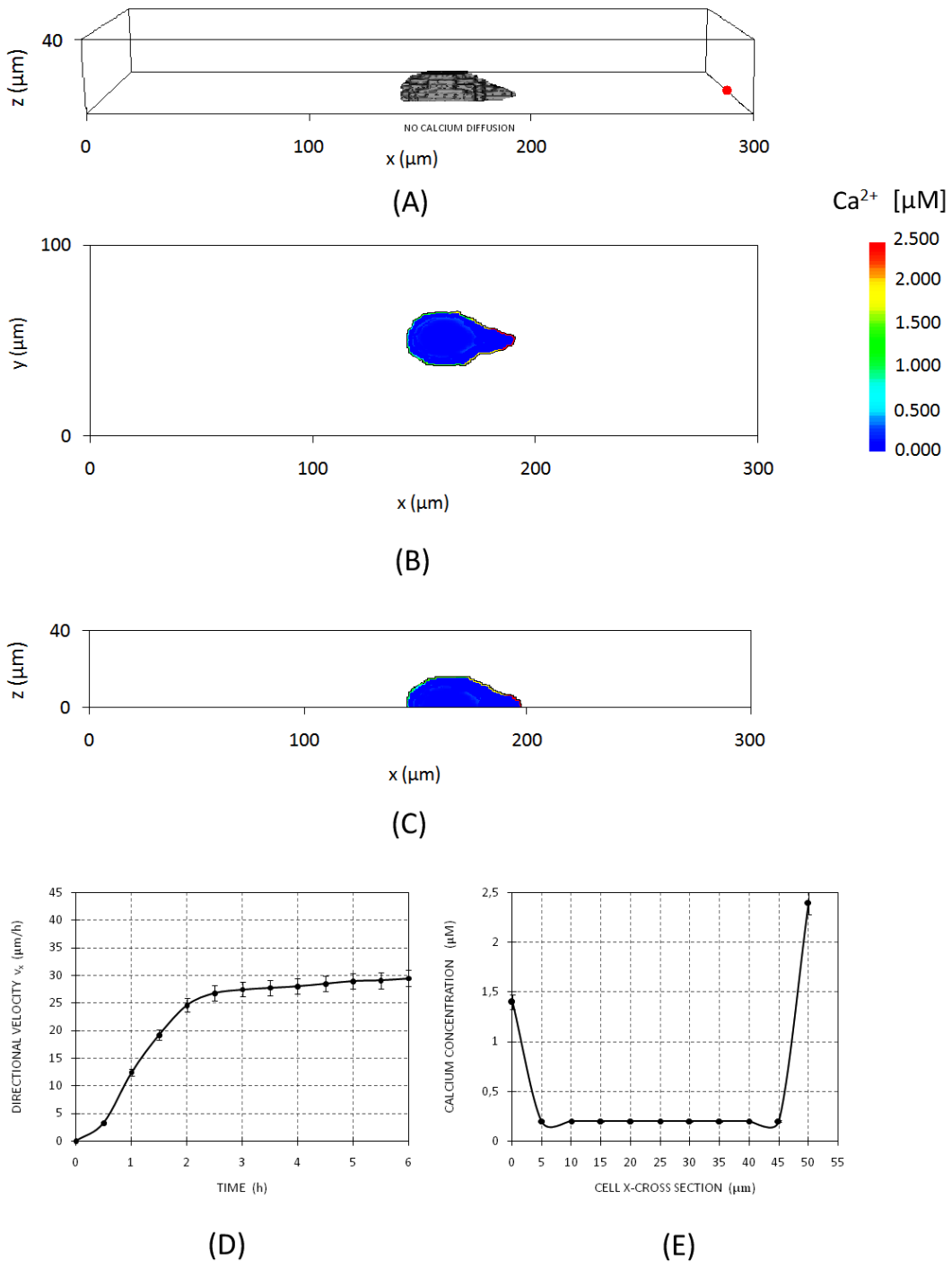

Figure 13: Cell migration with the exclusion of calcium diffusion ($D_{Ca} = 0$). (A) Three-dimensional view of cell position at t=6 h, red dot represents the VEGF source. Contour plots showing the final intracellular calcium concentrations in (B) z=1 μm plane and (C) y=50 μm plane. Calcium concentration has been pseudocolor-scaled so that the maximum value is red. (D) Evolution in time of cell directional velocity v_x. (E) Ca^{2+} concentration profiles at the end of migration, $t = 6$ h, along cell x-cross-section of the z=1 μm plane from the trailing edge to the leading edge of the polarized cell. The cell is quicker to reach the maximal directional velocity. which has a lower maximal peak. Mean over 10 simulations, error bars represent standard deviation.

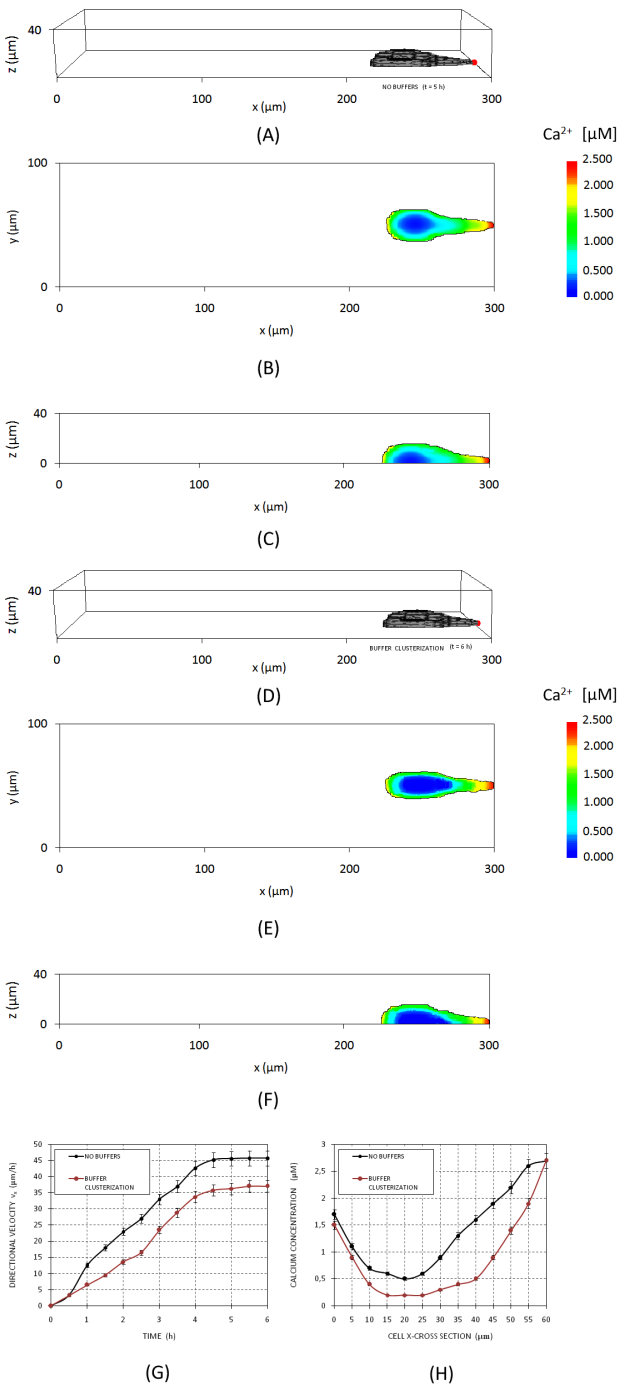

Figure 14: Cell migration with interference in the buffering process. (A) Three-dimensional view of cell position at t=5 h in the case of no buffers with the relative intracellular calcium profiles in (B) z=1 μm plane and (C) y=50 μm plane. (D) Three-dimensional view of cell position at t=6 h in the case of buffer clusterization, and relative contour plots of the final intracellular calcium concentration in (E) z=1 μm plane and (F) y=50 μm plane. In (A) and (D) red dot represents the VEGF source. (G) Evolution in time of cell directional velocity v_x in both cases. (H) Ca^{2+} concentration profiles at the end of migration, $t = 5$ h in the absence of buffers and $t = 6$ h in the case of clusterized buffers, along cell x-cross-section of the z=1 μm plane from the trailing edge to the leading edge of the polarized cell. Mean over 10 simulations, error bars represent standard deviation.

$$K_{buff}(\mathbf{x}) = \frac{K_{off}}{K_{off} + K_{on} b_T} \frac{d(\mathbf{x})}{d_0}, \tag{3.1}$$

where $d(\mathbf{x})$ and d_0 are the measures of the net euclidean distance from the PM of, respectively, site $\mathbf{x}$ and of the cell center of mass $\mathbf{x}_{CM}$. With respect to the standard case, also the proposed buffer clusterization does not strongly change the final spatial profile of calcium, but causes an increment of the maximal peak of responses at the tip of the motility structures (whose value is obviously the same as in the absence of buffers) and a decrement in the concentration of the ion in the more internal regions (i.e., the elevate presence of buffers almost blocks the diffusion of calcium, so that the zone with a basal level of the ion is bigger), see Fig. 14(E-F-H). Indeed, we have a steeper gradient of the intracellular Ca^{2+} level along the polarized axes of the cell, as illustrated in detail in Fig. 14(H). However, the total final calcium concentration remains almost elevate ($\widetilde{Ca}(t = 6 \text{ h}) \approx 3.2$), as well as the motile capability of the cell, as we do not observe a significant reduction in the maximal value of v_x and, consequently, a delay in the cell migration time, see Fig. 14(D-G).

MOLECULAR MECHANISM	MODEL PARAMETER	PEAK OF Ca^{2+} ACCUMULATION [μM]	RATE OF TOTAL Ca^{2+} ACCUMULATION	MAXIMAL DIRECTIONAL VELOCITY [μm/h]	FINAL CELL DISPLACEMENT [μm]
Ca^{2+} INFLUX	$F_{TOT}/2$	1.45	1.4	29.1	150
	$F_{TOT}/4$	1.02	0.6	17.8	70
	$F_{TOT}/8$	0.62	0.2	4.9	18
AA PRODUCTION	$k_{AA}=v_{Ca}=0$	1.06	1.2	22.7	110
NO PRODUCTION	$k_{NO}=v_{CaAA}=0$	1.56	1.6	30.5	180
CYTOSKELETAL REMODELING	$\lambda_2=50$	1.57	1.1	20.3	85
EXTENDED SOURCE		2.23	3.4	41.3	300
Ca^{2+} DIFFUSION	$D_{Ca}=0$	2.39	0.9	29.7	165
NO BUFFERS	$K_{buff}=1$	2.67	3.9 (in 5 hours)	46	300 (in 5 hours)
BUFFER CLUSTERIZATION	$K_{buff}=K_{buff}(\mathbf{x})$	2.67	3.2	36.8	300
CONTROL		2.28	3.6	42	300

Figure 15: Review of the proposed strategies interfering with cell motility. Second column gives the relative modified model parameters. The last four columns quantify each treatment by summarizing the critical parameters describing both the resulting calcium signals and the overall migratory ability of the EC. All values are mean over 10 simulations. Control solution represents the no treatment case, with no changes in the standard parameter setting, and corresponds to the simulations in Figs. 6 and 7.

In Fig. 15, we review all the proposed strategies to influence the phenomenology of the motile cell. In particular, we summarize the values of critical parameters quantifying both the VEGF-induced calcium signals and the resulting migratory properties of the EC.

4 Discussion

Calcium signaling represents a central mode for transducing information during a number of biological processes, including physiological and pathological neovascularization. In vascular endothelial cells, stimulations with angiogenic factors, such as VEGF isoforms, are in fact seen to trigger robust and reproducible calcium events (via the activation of second messenger arachidonic acid, AA, and nitric oxide, NO, cascades), which, in turn, mediate several mechanisms fundamental for cell migration, such cell polarization and increases in its intrinsic motility and chemotactic sensitivity. A number of mathematical approaches (both discrete [60, 61, 62], and continuous [92, 99]) have characterized the motion of vascular cells, as well as several techniques have treated calcium dynamics in different cell types [26, 42, 49, 93]. We have here combined such modules into an hybrid and multiscale framework, whose aim has been to analyze the complex relation between intracellular Ca^{2+} dynamics and the migratory phenomenology of a vascular EC. To achieve this goal, a modified version of a well-characterized model of proangiogenic calcium events [75], based on experimental data mainly obtained from electrophysiological experiments and single cell fluorimetric measurements, has been incorporated into a spatial-defined mesoscopic Cellular Potts Model. The CPM, in turn, has been characterized by a three-dimensional bicompartmentalized cell approximating the morphology of a real endothelial cell. Even if some other published CPM applications have used a compartmentalization approach for biological cells, which is also included as a standard possibility in the CompuCell3D package [4, 58, 101], we have made a further step forward introducing a set of compartments characterized by their immediate and direct correspondence to real subcellular elements, as this is the first time that a CPM accurately differentiates a cell in its nucleus and the cytosolic region (see also [91] form more details). Moreover, as a key features of our work, the interactions between the different levels have been explicitly modeled: the variation in cell-level biophysical and biomechanical properties, such as motility, chemotactic strength, and compressibility, given by the typical Potts parameters, have been in fact directly inherited from internal biochemical mechanisms.

The results of this multilevel approach have shown qualitative and quantitative agreement with empirical data, being capable of characterizing the proangiogenic calcium responses for their initiation site, propagation dynamic, and final pattern, as well as of capturing the phenomenological migration of a vascular cell, which has featured comparable directional velocity as experimental cultures, see [41]. In particular, the reproduction of the polarization process has had an high degree of resemblance to that of real vascular ECs observed, for example, in [23]. What confers value to our results is that such a cell behavior has been almost self-generating, as the only model artifact introduced in our approach has been the stiffness of the nucleus (i.e., its staking to the underlying lattice, see Section 3 for a detailed comment), which has resulted in its slow motion and in its lagging behind the cytosolic region. However, we have

not needed of other artificial rules beyond, such as predefined spatial information (for example a given target length, as done in [61]) or specific phenomenological rules associated to the different cell compartment. This provides the fact that a calcium-dependent elasticity of the cell cytosol, in conjunction with the presence of a rigid nucleus and of a local chemical stimulus, constitutes a sufficient set of minimal and simplified requirements for the cell transition from a symmetric stationary morphology to a polarized mobile state. Another correct aspect that has emerged has been the distribution of the intracellular calcium concentration, which has closely reproduced experimental observations in [98]. Pro-angiogenic calcium responses have been found to inhomogeneously propagate from the sub-plasma membrane regions to the whole cells, leading to a strongly localized final pattern. Higher cytosolic calcium accumulations have in fact been restricted in the thinner motility structures of the leading front of the EC (i.e., either pseudopodia or lamellipodia), while their peaks decrease in the thicker central/nuclear region. These considerations have clearly demonstrated that local levels of the ion are strictly geometric-dependent. This heterogeneity is highly relevant during angiogenic progression, when ECs constantly reorganize their shape, and explains the reason why cells expressing the same amount of channel have different response to analogous stimulations. Moreover, several reports suggest that the transcriptional pattern of specific genes during vascular progression critically depends on the spatio-temporal calcium dynamics [22, 25]. This model has also confirmed the efficiency some current anti-angiogenic therapies (such as the use of CAI, L-NAME, and AACOCF3 drugs [67, 76, 98]), suggested novel and experimentally testable strategies, as the block of actin-myosin interaction with phalloidin-like compounds, and proposed non-intuitive, currently unavailable but potentially interesting way to stop cell locomotion by interfering with calcium signaling mechanisms, such as the inhibition of intracellular calcium diffusion, see Fig. 15 for a useful review.

In our opinion, this study is a big step towards a multiscale integration between a discrete cellular-level approach and a continuous subcellular-level model. However, it contains a number of assumptions. In fact simplifications have been made to minimize the number of interacting molecular components within the model, and thus to limit its size and the spatial complexity: the reason has been the improvement of its computational efficiency, while maintaining the accuracy of simulations. For example, the model has been facilitated, in the considered precise range of VEGF stimulation (micromolar levels, < 5 μM), by the absence of other possible mechanisms for calcium signalling than the nonstore-operated calcium entry (NSOCE), such as calcium-induced calcium release via ryanodine receptor and calcium release from intra-cellular stores. Moreover, PM channels and pumps have been modeled as uniformly distributed over the entire cell surface, and several membrane-localized signal transduction proteins, that are known intermediates in AA and NO generation, such as PLA2 and eNOS, have not been included. We have also assumed that cell adhesion mechanisms, as the coordinated development and release of focal adhesions (FAs), a basic requirement for cell movement, were energetically neutral. In this way, we have considered the chemotactic stimulus as the only

cause of cell directional migration.

Finally, if a number of parameters of the model, such as diffusion coefficients, channel and pump kinetics, and endogenous buffers, have been taken from the literature and are specifically referred to ECs, others have been derived from experiments with different cell lines and experimental conditions. However, they have been constrained in a range consistent with our own system. Eventually, when a parameter was not available, it has been estimated within reasonable biophysical constraints, see Appendix for details.

The two parts the model is formed by can be still improved working in several directions. A natural development of the discrete CPM will be the incorporation of a description of the kinetics of the cytoskeletal remodeling. The present version of the model in fact does not focus on the dynamics of actin filaments, but rather considers the cell cytosol as a single elastic body undergoing local mechanical stresses, due to thermodynamic forces and chemical stimuli, on its membrane. A more detailed multiscale model would combine both approaches, using the stress distributions at the PM as a signaling input for the subsequent polimerization process of the actin cytoskeleton. The introduction of the dynamics of the cell cytoskeleton would result also in a more accurate description of the movement of cell nucleus. As explained in Sec. 3, its motion is in fact characterized by two well-defined contributions, approached in the presented method with a simplified picture: a negligible autonomous fluctuation within the cytoplasmatic fluid and the drag movement due to the interactions with the matrix substrate, mediated by intermediate filaments and microtubules, which could be more realistically described by an explicit model of the actin component of the cell cytoskeleton. Moreover, the description of the VEGF-induced calcium dynamics will be greatly improved by more constraints obtained mainly by biochemical quantitative measurements. In particular, a more detailed quantitative description of the molecular machinery underlying AA and NO release, as well as further structural and functional information on calcium channels and pumps would be very useful. In particular, this model is based on the hypothesis of two independent channels (AA- or NO-activated), but we cannot exclude neither the existence of channels co-modulated by AA and NO nor potential cross regulations between different channel types: for example, several member of the TRP family (in particular TRPC and TRPV sub-families) can be also involved in the proangiogenic signals [50, 74, 77]. All these refinements will also help to ascertain more accurate parameter values for the model, to quantitatively test its predictions and to ensure that it is biologically realistic.

A further interesting model development will be its extension to a population of vascular ECs, simulating either an *in vitro* tubulogenic assay, or an *in vivo* angiogenic progression. These approaches could in fact provide a deep analysis on how the biochemical and biomechanical processes modeled here influence the overall formation of a malignant vasculature. Obviously this model extension will require the inclusion of several other biological mechanisms, such as cell proliferation (which has not been included in this work since the temporal scale involved here is much lower

than the typical duration of a cell cycle, $\gg$ 6 hours) and differentiation, as well as cell-cell adhesive interactions and contact inhibition of growth.

Acknowledgments

WE GRATEFULLY ACKNOWLEDGE DISCUSSIONS WITH PROF. LUIGI PREZIOSI FROM THE DEPARTMENT OF MATHEMATICS, POLITECNICO DI TORINO, AND WITH PROF. LUCA MUNARON AND DR. EMANUELA PUPO FROM THE DEPARTMENT OF ANIMAL AND HUMAN BIOLOGY, UNIVERSITA' DEGLI STUDI DI TORINO, ON MANY ASPECTS OF THIS WORK. MS WAS PARTIALLY FUNDED BY THE ITALIAN MINISTRY OF UNIVERSITY AND RESEARCH UNDER A GRANT ON "MATH MODELS OF THE INTERACTIONS BETWEEN CELLS AND ENVIRONMENT" AND BY FONDAZIONE CREDITO DI RISPARMIO DI TORINO (CRT) THROUGH A "LAGRANGE PROJECT FELLOWSHIP".

A Appendix - Parameter Estimates

Many values of parameters used in the model have been inferred from experimental measurements on various endothelial cell lineages. Therefore, we have assembled parameter estimates based on a composite set of data. However, we have observed that the behavior of the model is fairly robust in large regions of parameter space around our estimates, leading to confidence in the biological relevance of results, which have been also confirmed by quantitative comparisons with *in vitro* results. A summary of parameter values used in the model has been done in Tables I, II and III. In this Appendix we give details of how we have calculated these estimates.

A.1 Parameter Estimates of the Discrete Extended Cellular Potts Model

Given the energetic nature of the CPM, a direct one-to-one correspondence between the CPM parameters and the experimental quantities is not straightforward (see also reviews [33, 63] for a comment). However, it is possible to realistically and accurately infer these values by deriving empirical relationships with *in vitro* measurements. The model parameters related to the basal (i.e. in the unstimulated case) motility properties of the cell, T_0 (the size of cell membrane fluctuation in resting conditions) and $\mu_{pers,0}$ (the basal persistence parameter) have been estimated with a quantitative comparison with experimental analysis. In particular, we have computed the displacement d covered in a 3 hours time-lapse by the cell in *control conditions* (which is simply $d = \mathbf{x}(t = 3 \text{ h}) - \mathbf{x}(t = 0)$, where $\mathbf{x}$ is the position of the cell center of mass), and have fitted this value with analogous measurements for EC autonomous motility in embryonic mouse allantoides, made in [81]. The values in the parameter space that have lead to the optimal empirical fitting to *in vitro* data were $T_0 = 3.5$ and $\mu_{pers,0} = 0.8$, see Fig. 16.

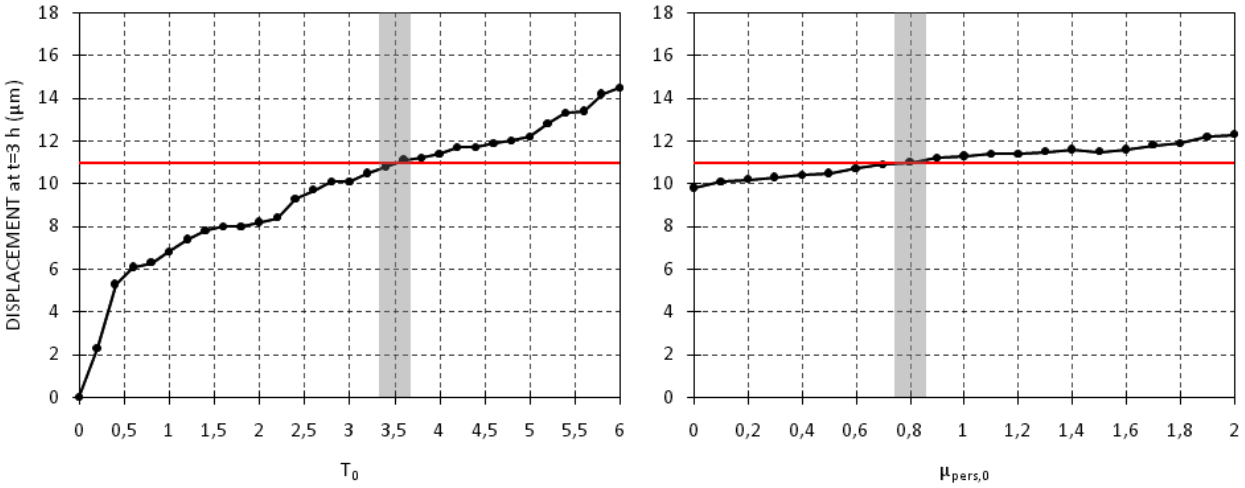

Figure 16: Effective displacement ($d = \mathbf{x}(t = 3\,\text{h}) - \mathbf{x}(t = 0)$, where $\mathbf{x}$ is the position of the cell center of mass) of unstimulated vascular endothelial cell in a 3 hours time lapse for experimental (red line, see [81]) and simulated (black line) case. Mean values over 10 simulations. Left plot has been used to estimate the intrinsic motility of the cell T_0, right plot to estimate its basal persistence time $\mu_{pers,0}$.

$\mu_{ch,0}$ is the intrinsic chemotactic strength of the cell, which has no influence in control conditions, since, without VEGF stimulation, $\Delta H_{chemotaxis} = 0$ (see Eq. (2.7)). As biological measurements were not available, we have tried a wide range of low values and selected $\mu_{ch,0} = 0.2$, assuming that the chemical sensitivity of the cell is strongly increased by cytosolic calcium ions. T_1 is instead linked to the motility of the cell nucleus. In particular, low values of T_1 translate to small nuclear membrane fluctuation, which is biologically reasonable (see Sec 3 for a detailed explanation). As experimental data on nuclear membrane fluctuations were not available, we have experimented with a large range of values, before settling on $T_1 = 0.25$. μ_1 and λ_1 concern the growth and the deformation ability of the cell nucleus. We have not found yet a way to determine them directly from experimental data, since the the biomechanical properties of cell nuclei have, until now, received little attention. However, we have used the high values of $\mu_1 = \lambda_1 = 20$ to keep the stochastic geometrical fluctuations of the nuclear cluster almost negligible. μ_2 regulates endothelial cell growth, but it does not directly influence its phenomenology. Since we have not included in the model any nutrients, after some trials, we have set $\mu_2 = 20$. This in order to keep fluctuations in cell volume within a few percent. The parameter $\lambda_{2,0}$ is related to the basal compressibility of the cell (i.e in the absence of any endogenous chemical stimulation or force): observing that resting EC maintained their initial geometrical configuration, with negligible changes of shape or cytoskeletal active reorganization, we have chosen $\lambda_{2,0} = 1.2$. The parameter $J_{1,2}$ is related to the generalized adhesion between the nuclear cluster and the cytosolic region. It prevents the EC compartments from disconnecting, however it has a limited effect on the cell dynamics. We have chosen a high $J_{1,2} = -20$.

A.2 Parameter Estimates of the Continuous Models of VEGF-Induced Calcium-Dependent Biochemical Mechanisms

VEGF diffusion $D_V = 10\ \mu\text{m}^2\text{s}^{-1}$ and decay $\lambda_V = 1.8 \cdot 10^{-4}\ \text{s}^{-1}$ have been quoted in [92]. $\beta_V(t)$, the maximal amount of VEGF molecules that can be locally (i.e. per site) bound and internalized by the EC for unit of time has been estimated following [6, 56]. In particular, for the computation of $\beta_V(t)$, we have considered a spatially homogeneous average number of VEGF receptors per cell membrane site, which has been estimated by dividing the total number of VEGF receptor in a generic endothelial cell, considered constant and equal to 311.200 (as measured in [102] for human colonic ECs), for the actual extension of the EC membrane, which is initially equal to 2700 μm^2 [98]. The local number of VEGF receptor thus varies in time: however, to avoid further overcomplication, we have not taken into account of other time-dependent phenomena, such as receptor clusterization. Moreover we have taken into account an instantaneous VEGF-receptor complex internalization rate of $4.3 \cdot 10^{-4}$ per second [55], and 45 kDa as the molecular weight for a VEGF molecule [17].

We have taken the cytosolic diffusion parameter of AA, $D_{AA} = 10\ \mu\text{m}^2\text{s}^{-1}$, and its degradation rate, $\lambda_{AA} = 30\ \text{s}^{-1}$ from [75], where they have been estimated fitting experimental measurements made by the same group on bovine aortic endothelial cells [67]. The Michaelis-Menten coefficients $k_{AA} = 30\ \mu\text{Ms}^{-1}$ and $K_{AA} = 1\ \mu\text{M}$ of the VEGF receptor-mediated production of AA have been chosen for the best fit with experimental measures made for the same theoretical paper [75]. The Ca^{2+}-induced AA release has been modeled with another saturable Michaelis-Menten function: in the absence of more precise experimental data we have set $v_{Ca} = 0.5 \cdot v_{CaAA}$ and $c_{AA} = c_{NO}$ (for the values of v_{CaAA} and c_{NO} see below). With these approximated values we have assumed that the calcium-dependent biosynthesis of both AA and NO happen at comparable rates and time scales.

The intracellular NO diffusion has been taken to be $D_{NO} = 3300\ \mu\text{m}^2\text{s}^{-1}$: it has been calculated in [52] and used also in [75]. The coefficient of NO degradation $\lambda_{NO} = 0.1\ \text{s}^{-1}$ has been evaluated in [75]. Since few data were available for the VEGF receptor-mediated production of NO we have used $k_{NO} = k_{AA}$ and $K_{NO} = K_{AA}$. The production of NO regulated by both AA and Ca^{2+} has been also described by a classical Michaelis-Menten function: $v_{CaAA} = 1.5\ \mu\text{Ms}^{-1}$, the maximal rate of NO release, has been estimated by fitting the time course of NO production experimentally measured using fluorescent probes and selective electrodes in [14, 67]. The dissociation constants between Ca^{2+} and eNOS, $c_{NO} = 0.3\ \mu\text{M}$, and between AA and eNOS, $a_{AA} = 0.2\ \mu\text{M}$, have been also taken from [75, 83].

The local resting cytosolic Ca^{2+} concentration, Ca_0 = 0.05 μM, and the external calcium concentration, $Ca_{ext,0}$ = 2000 μM, have been assumed uniform and taken from experimental [10] and theoretical [75] works. The calcium diffusion coefficient $D_{Ca} = 220\ \mu\text{m}^2\text{s}^{-1}$ has been well characterized in literature for several cell lines [26, 46, 75]. Several authors model the Ca^{2+} efflux as a sum of Hill functions [75, 100]. We have approximated this by a single Michaelis-Menten term, with coefficients $k_{Ca} = 24.7\ \mu\text{Ms}^{-1}$, the maximal rate of extrusion, and $Ca_{out} = 0.32\ \mu\text{M}$, the calcium concentration at which the rate of exchange is half maximal, chosen to fit those Hill-type curves over a physiological range of calcium concentration. The calcium entry through AA- and NO-sensitive channels has been described by saturable Michaelis-Menten relations, where $F_{AA,max}$ and $F_{NO,max}$ are the maximal possible influx rates. q_{AA} and q_{NO} are the concentrations of AA and NO responsible for the half

maximal activation of the respective channels. All these parameters have been chosen to fit the calcium-permeable channel currents obtained by patch clamp experiments in [67, 75]. The rates of buffering and debuffering of Ca^{2+} to intracellular proteins have been measured by several experimental works. In particular, we have used $K_{on} = 100\ \mu\text{M}^{-1}\text{s}^{-1}$ and $K_{off} = 300\ \text{s}^{-1}$ from [8]. The total concentration of calcium binding sites in the cytosol has instead been estimated to be $b_T = 450\ \mu\text{M}$, accordingly to [26, 75].

References

[1] Alberts, B., Bray, D., Lewis, J., Raff, M., Roberts, K., Watson, J. D., 1994. *Molecular Biology of the Cell, 3rd edition.* Garland Science.

[2] Albrecht, M. A., Colegrove, S. L., Friel, D. D., 2002. *Differential regulation of ER Ca2+ uptake and release rates accounts for multiple modes of Ca2+-induced Ca2+ release.* J Gen Physiol, 119 (3), 211 - 233.

[3] Ambrosi, D., Bussolino F., Preziosi, L., 2005. *A review of vasculogenesis models.* J Theor Med, 6 (1), 1 - 19.

[4] Balter, A., Merks, R. M. H., Poplawski, N. J., Swat, M., Glazier, J. A., 2007. *The Glazier-Graner-Hogeweg model: extensions, future directions, and opportunities for further study.* In A. R. A. Anderson, M. A. J. Chaplain, and K. A. Rejniak editors, *Single-Cell-Based Models in Biology and Medicine*, Mathematics and Biosciences in Interactions, Birkaüser, 157 - 167.

[5] Barbiero, G., Munaron, L., Antoniotti, S., Baccino, F. M., Bonelli, G., Lovisolo, D., 1995. *Role of mitogen-induced calcium influx in the control of the cell cycle in Balb-c 3T3 fibroblasts.* Cell Calcium, 18 (6), 542 – 556.

[6] Bauer, A. L., Jackson, T. L., Jiang, Y., 2007. *A cell-based model exhibiting branching and anastomosis during tumor-induced angiogenesis.* Biophys J, 92 (9), 3105 - 3121.

[7] Bauer, K. S., Cude, K. J., Dixon, S. C., Kruger, E. A., Figg, W. D., 2000. *Carboxyamido-triazole inhibits angiogenesis by blocking the calcium-mediated nitric-oxide synthase-vascular endothelial growth factor pathway.* J Pharmacol Exp Ther, 292 (1), 31 – 37.

[8] Bayley, P., Ahlström, P., Martin, S. R., Forsen S., 1984. *The kinetics of calcium binding to calmodulin: Quin 2 and ANS stopped-flow fluorescence studies.* Biochem Biophys Res Commun, 120 (1), 185 – 191.

[9] Bennett, J., Weeds, A., 1986. *Calcium and the cytoskeleton.* Br Med Bull, 42 (4), 385 - 390.

[10] Berridge, M. J., Bootman, M. D., Roderick, H. L., 2003. *Calcium signalling: dynamics, homeostasis and remodelling.* Nat Rev Mol Cell Biol, 4 (7), 517 - 529.

[11] Berridge, M. J., 1995. *Calcium signalling and cell proliferation.* Bioessays, 17 (6), 491 - 500.

[12] Berridge, M. J., Lipp, P., Bootman, M. D., 2000. *The versatility and universality of calcium signalling.* Nat Rev Mol Cell Biol, 1 (1), 11 - 21.

[13] Berridge, M. J., Bootman, M. D., Lipp, P., 1998. *Calcium – a life and death signal.* Nature, 395 (6703), 645 - 648.

[14] Blatter, L. A., Taha, Z., Mesaros, S., Shacklock, P. S., Wier, W. G., Malinski, T., 1995. *Simultaneous measurements of Ca2+ and nitric oxide in bradykinin-stimulated vascular endothelial cells.* Circ Res, 76 (5), 922 - 924.

[15] Bootman, M. D., Lipp, P., Berridge, M. J., 2001. *The organization and functions of local Ca2+ signals.* J Cell Sci, 114 (12), 2213 - 2222.

[16] Bussolino, F., Arese, M., Audero, E., Giraudo, E., Marchio, S., Mitola, S., Primo, L., Serini, G., 2003. *Biological aspects in tumor angiogenesis.* In L. Preziosi editor, *Cancer modeling and simulation*, Mathematical Biology and Medicine Sciences, CRC Press, 1 - 16.

[17] Carmeliet, P., Jain, R. K., 2000. *Angiogenesis in cancer and other diseases.* Nature, 407 (6801), 249 - 257.

[18] Carmeliet, P., 2005. *VEGF as a key mediator of angiogenesis in cancer.* Oncology, 69 (3), 4 - 10.

[19] A. Chauviere, L. Preziosi, and C. Verdier editors, *Cell mechanics: from single scaled-based models to multscale modeling*, Mathematical and Computational Biology Series, CRC Press.

[20] Clapham, D. E., 2007. *Calcium signalling.* Cell, 131 (6), 1047 - 1058

[21] Coatesworth, W., Bolsover, S., 2008. *Calcium signal transmission in chick sensory neurones is diffusion based.* Cell Calcium, 43 (3), 236 - 249.

[22] Dolmetsch, R. E., Xu, K., Lewis, R. S., 1998. *Calcium oscillations increase the efficiency and specificity of gene expression.* Nature, 392 (6679), 933 - 936.

[23] Drake, C. J., LaRue, A., Ferrara, N., Little, C. D., 2000. *VEGF regulates cell behavior during vasculogenesis.* Dev Biol, 224 (2), 178 - 188.

[24] Etienne-Manneville, S., 2004. *Cdc42 - the centre of polarity.* J Cell Sci, 117 (Pt 8), 1291 - 1300.

[25] Feske, S., Giltnane, J., Dolmetsch, R., Staudt, L. M., Rao, A., 2001. *Gene regulation mediated by calcium signals in T lymphocytes.* Nat Immunol, 2 (4), 316 - 324.

[26] Fink, C. C., Slepchenko, B., Moraru, I. I., Watras, J., Schaff, J. C., Loew, L. M., 2000. *An image-based model of calcium waves in differentiated neuroblastoma cells.* Biophys J, 79 (1), 163 - 183.

[27] Fiorio Pla, A., Grange, C., Antoniotti, S., Tomatis, C., Merlino, A., Bussolati, B., Munaron, L., 2008. *Arachidonic acid-induced Ca2+ entry is involved in early steps of tumor angiogenesis.* Mol Cancer Res, 6 (4), 535 - 545.

[28] Fiorio Pla, A., Munaron, L., 2001. *Calcium influx, arachidonic acid, and control of endothelial cell proliferation.* Cell Calcium, 30 (4), 235 - 244.

[29] Fiorio Pla, A., Genova, T., Pupo, E., Tomatis, C., Genazzani, A., Zaninetti, R., Munaron, L., 2010. *Multiple roles of protein kinase a in arachidonic acid-mediated Ca2+ entry and tumor-derived human endothelial cell migration.* Mol Cancer Res, 8 (11), 1466 – 1476.

[30] Fleming, I., Busse, R., 1999. *Signal transduction of eNOS activation.* Cardiovasc Res, 43 (3), 532 - 541.

[31] Funamoto, S., Meili, R., Lee, S., Parry, L., Firtel, R. A., 2002. *Spatial and temporal regulation of 3-phosphoinositides by PI 3-kinase and PTEN mediates chemotaxis.* Cell, 109 (5), 611 - 623.

[32] Gerhardt, H., Golding, M., Fruttiger, M., Ruhrberg, C., Lundkvist, A., Abramsson, A., Jeltsch, M., Mitchell, C., Alitalo, K., Shima, D., Betsholtz, C., 2003. *VEGF guides angiogenic sprouting utilizing endothelial tip cell filopodia.* J Cell Biol, 161 (6), 1163 - 1177.

[33] Glazier, J. A., Balter, A., Poplawski, N. J., 2007. *Magnetization to morphogenesis: A brief history of the Glazier-Graner-Hogeweg model.* In A. R. A. Anderson, M. A. J. Chaplain, and K. A. Rejniak editors, *Single-Cell-Based Models in Biology and Medicine*, Mathematics and Biosciences in Interactions, Birkaüser, 79 - 106.

[34] Glazier, J. A., Graner, F., 1993. *Simulation of the differential adhesion driven rearrangement of biological cells*. Phys Rev E Stat Phys Plasmas Fluids Relat Interdiscip Topics, 47 (3), 2128 - 2154.

[35] Goto, Y., Miura, M., Iijima, T., 1996. *Extrusion mechanisms of intracellular Ca2+ in human aortic endothelial cells.* Eur J Pharmacol, 314 (1-2), 185 - 192.

[36] Graner, F., Glazier, J. A., 1992. *Simulation of biological cell sorting using a two dimensional extended Potts model.* Phys Rev Lett, 69 (13), 2013 - 2016.

[37] Haugh, J. M., Codazzi, F., Teruel, M., Meyer, T., 2000. *Spatial sensing in fibroblasts mediated by 3' phosphoinositides.* J Cell Biol, 151 (6), 1269 - 1280.

[38] Hong, D., Jaron, D., Buerk, D. G., Barbee, K. A., 2008. *Transport-dependent calcium signaling in spatially segregated cellular caveolar domains.* Am J Physiol Cell Physiol, 294 (3), C856 – C866.

[39] Howard, J., 2001. *Mechanics of motor proteins and the cytoskeleton.* Sinauer Associates, Inc., Sunderland, MA.

[40] Hryshko, L. V., Philipson, K. D., 1997. *Sodium-calcium exchange: recent advances.* Basic Res Cardiol, 92 (1), 45 - 51.

[41] Huang, S., Brangwynne, C. P., Parker, K. K., Ingber, D. E., 2005. *Symmetry-breaking in mammalian cell cohort migration during tissue pattern formation: role of random-walk persistence.* Cell Motil Cytoskeleton, 61 (4), 201 - 213.

[42] Hunding, A., Ipsen, M., 2003. *Simulation of waves in calcium models with 3D spherical geometry.* Math Biosci, 182 (1), 45 - 66.

[43] Kahl, C. R., Means, A. R., 2003. *Regulation of cell cycle progression by calcium/calmodulin-dependent pathways.* Endocr Rev, 24 (6), 719 - 736.

[44] Khanapure, S. P., Garvey, D. S., Janero, D. R., Gordon Letts, L., 2007. *Eicosanoids in inflammation: biosynthesis, pharmacology, and therapeutic frontiers.* Curr Top Med Chem, 7 (3), 311 - 340.

[45] Kimura, H., Esumi, H., 2003. *Reciprocal regulation between nitric oxide and vascular endothelial growth factor in angiogenesis.* Acta Biochim Pol, 50 (1), 49 - 59.

[46] Klingauf, J., Neher, E., 1997. *Modeling buffered Ca2+ diffusion near the membrane: implications for secretion in neuroendocrine cells.* Biophys J, 72 (2 Pt 1), 674 - 690.

[47] Kohn, E. C., Sandeen, M. A., Liotta, L. A., 1992. *In vivo efficacy of a novel inhibitor of selected signal transduction pathways including calcium, arachidonate, and inositol phosphates.* Cancer Res, 52 (11), 3208 – 3212.

[48] Kohn, E. C., Liotta, L. A., 1990. *L651582: a novel antiproliferative and antimetastasis agent.* J Natl Cancer Inst, 82 (1), 54 – 60.

[49] Kraus, M., Wolf, B., Wolf, B., 1996. *Crosstalk between cellular morphology and calcium oscillation patterns. Insights from a stochastic computer model.* Cell Calcium, 19 (6), 461 - 472.

[50] Kwan, H.-Y., Huang, Y., Yao, X., 2007. *TRP channels in endothelial function and dysfunction.* Biochim Biophys Acta, 1772 (8), 907 - 914.

[51] Jafri, M. S., Keizer, J., 1995. *On the roles of Ca2+ diffusion, Ca2+ buffers, and the endoplasmic reticulum in IP3-induced Ca2+ waves.* Biophys J, 69 (5), 2139 - 2153.

[52] Lancaster, J. R. Jr, 1997. *A tutorial on the diffusibility and reactivity of free nitric oxide.* Nitric Oxide, 1 (1), 18 - 30.

[53] Lin, S., Fagan, K. A., Li, K.-X., Shaul, P. W., Cooper, D. M. F., Rodman, D. M., 2000. *Sustained endothelial nitric oxide synthase activation requires capacitative Ca2+ entry.* J Biol Chem, 275 (24), 17979 - 17985.

[54] Lovisolo, D., Distasi, C., Antoniotti, S., Munaron, L., 1997. *Mitogens and calcium channels.* News Physiol Sci, 12, 279 – 285.

[55] Mac Gabhann, F., Popel, A. S., 2004. *Model of competitive binding of vascular endothelial growth factor and placental growth factor to VEGF receptors on endothelial cells.* Am J Physiol Heart Circ Physiol, 286 (1), H153 - H164.

[56] Mahoney, A. W., Smith, B. G., Flann, N. S., Podgorski, G. J., 2008. *Discovering novel cancer therapies: a computational modeling and search approach.* IEEE conference on Computational Intelligence in Bioinformatics and Bioengineering, 233 - 240.

[57] Marée, A. F. M., Grieneisen, V. A., Hogeweg, P., 2007. *The Cellular Potts Model and biophysical properties of cells, tissues and morphogenesis*. In A. R. A. Anderson, M. A. J. Chaplain, and K. A. Rejniak editors, *Single-Cell-Based Models in Biology and Medicine*, Mathematics and Biosciences in Interactions, Birkaüser, 107 - 136.

[58] Marée, A. F. M., Jilkine, A., Dawes, A., Grieneisen, V. A., Edelstein-Keshet, L., 2006. *Polarization and movement of keratocytes: A multiscale modelling approach.* Bull Math Biol, 68 (5), 1169 – 1211.

[59] Meili, R., Firtel, R. A., 2003. *Two poles and a compass.* Cell, 114 (2), 153 - 156.

[60] Merks, R. M. H., Glazier, J. A., 2006. *Dynamic mechanisms of blood vessel growth.* Nonlinearity, 19 (1), C1 - C10.

[61] Merks, R. M. H., Brodsky, S. V., Goligorksy, M. S., Newman, S. A., Glazier, J. A., 2006. *Cell elongation is key to in silico replication of in vitro vasculogenesis and subsequent remodeling.* Dev Biol, 289 (1), 44 - 54.

[62] Merks, R. M. H., Perryn, E. D., Shirinifard, A., Glazier, J. A., 2008. *Contact-inhibited chemotactic motility: role in de novo and sprouting blood vessel growth.* PLoS Comput Biol, 4 (9), e1000163.

[63] Merks, R. M. H., Koolwijk, P., 2009. *Modeling morphogenesis in silico and in vitro: towards quantitative, predictive, cell-based modeling.* Math Model Nat Phenom, 4 (4), 149 - 171.

[64] Metropolis, N., Rosenbluth, A. W., Rosenbluth, M. N., Teller, A. H., Teller, E., 1953. *Equation of state calculations by fast computing machines.* J Chem Phys, 21 (6), 1087 - 1092.

[65] Mittara, S., Ulyatt, C., Howell, G. J., Bruns, A. F., Zachary, I., Walker, J. H., Ponnambalam, S., 2009. *VEGFR1 receptor tyrosine kinase localization to the Golgi apparatus is calcium-dependent.* Exp Cell Res, 315 (5), 877 – 889.

[66] Moccia, F., Berra-Romani, R., Baruffi, S., Spaggiari, S., Signorelli, S., Castelli, L., Magistretti, J., Taglietti, V., Tanzi, F., 2002. *Ca2+ uptake by the endoplasmic reticulum Ca2+ - ATPase in rat microvascular endothelial cells.* Biochem J, 364 (1), 235 - 244.

[67] Mottola, A., Antoniotti, S., Lovisolo, D., Munaron, L., 2005. *Regulation of noncapacitative calcium entry by arachidonic acid and nitric oxide in endothelial cells.* FASEB J, 19 (14), 2075 - 2077.

[68] Munaron, L., 2002. *Calcium signalling and control of cell proliferation by tyrosine kinase receptors (review).* Int J Mol Med, 10 (6), 671 - 676.

[69] Munaron, L., 2006. *Intracellular calcium, endothelial cells and angiogenesis.* Recent Pat Anticancer Drug Discov, 1 (1), 105 - 119.

[70] Munaron, L., Antoniotti, S., Distasi, C., Lovisolo, D., 1997. *Arachidonic acid mediates calcium influx induced by basic fibroblast growth factor in Balb-c 3T3 fibroblasts.* Cell Calcium, 22 (3), 179 - 188.

[71] Munaron, L., Antoniotti, S., Fiorio Pla, A., Lovisolo, D., 2004. *Blocking Ca2+ entry: a way to control cell proliferation.* Curr Med Chem, 11 (12), 1533 - 1543.

[72] Munaron, L., Antoniotti, S., Lovisolo, D., 2004. *Intracellular calcium signals and control of cell proliferation: how many mechanisms?* J Cell Mol Med, 8 (2), 161 - 168.

[73] Munaron, L., Fiorio Pla, A., 2000. *Calcium influx induced by activation of tyrosine kinase receptors in cultured bovine aortic endothelial cells.* J Cell Physiol, 185 (3), 454 - 463.

[74] Munaron, L., Tomatis, C., Fiorio Pla, A., 2008. *The secret marriage between calcium and tumor angiogenesis.* Technol Cancer Res Treat, 7 (4), 335 - 339.

[75] Munaron, L., 2009. *A tridimensional model of proangiogenic calcium signals in endothelial cells.* The Open Biology Journal, 2, 114 - 129.

[76] Munaron, L., Fiorio Pla, A., 2009. *Endothelial calcium machinery and angiogenesis: understanding physiology to interfere with pathology.* Curr Med Chem, 16 (35), 4691 - 4703.

[77] Nilius, B., Droogmans, G., 2001. *Ion channels and their functional role in vascular endothelium.* Physiol Rev, 81 (4), 1415 - 1459.

[78] Nobes, C. D., Hall, A., 1999. *Rho GTPases control polarity, protrusion, and adhesion during cell movement.* J Cell Biol, 144 (6), 1235 - 1244.

[79] Pacher, P., Beckman, J. S., Liaudet, L., 2007. *Nitric oxide and peroxynitrite in health and disease.* Physiol Rev, 87 (1), 315 - 424.

[80] Patton, A. M., Kassis, J., Doong, H., Kohn, E. C., 2003. *Calcium as a molecular target in angiogenesis.* Curr Pharm Des, 9 (7), 543 - 551.

[81] Perryn, E. D., Czirók, A., Little, C. D., 2008. *Vascular sprout formation entails tissue deformations and VE-cadherin dependent cell-autonomous motility.* Dev Biol, 313 (2), 545 - 555.

[82] Pollard, T. D., Borisy, G. G., 2003. *Cellular motility driven by assembly and disassembly of actin filaments.* Cell, 112 (4), 453 - 465.

[83] Pollock, J. S., Förstermann, U., Mitchell, J. A., Warner, T. D., Schmidt, H. H. H. W., Nakane, M., Murad, F., 1991. *Purification and characterization of particulate endothelium-derived relaxing factor synthase from cultured and native bovine aortic endothelial cells.* Proc Natl Acad Sci USA, 88 (23), 10480 - 10484.

[84] Poplawski, N. J., Shirinifard, A., Swat, M., Glazier, J. A., 2008. *Simulation of single-species bacterial-biofilm growth using the Glazier-Graner-Hogeweg model and the CompuCell3D modeling environment*. Math Biosci Eng, 5 (2), 355 - 388.

[85] Rafelski, S. M., Theriot, J. A., 2004. *Crawling toward a unified model of cell motility: spatial and temporal regulation of actin dynamics.* Annu Rev Biochem, 73, 209 - 239.

[86] Rizzuto, R., Duchen, M. R., Pozzan, T., 2004. *Flirting in little space: the ER/mitochondria Ca2+ liaison.* Sci STKE, 2004 (215), re1.

[87] Santella, L., 1998. *The role of calcium in the cell cycle: facts and hypotheses.* Biochem Biophys Res Commun, 244 (2), 317 - 324.

[88] Savill, N. J., Hogeweg, P., 1997. *Modeling morphogenesis: from single cells to crawling slugs*. J Theor Biol, 184, 229 – 235.

[89] Scianna, M., Merks, R. M. H., Preziosi, L., Medico, E., 2009. *Individual cell-based models of cell scatter of ARO and MLP-29 cells in response to hepatocyte growth factor.* J Theor Biol, 260 (1), 151 - 160.

[90] Scianna, M., Munaron, L., Preziosi, L., 2011. *A multiscale hybrid approach for vasculogenesis and related potential blocking therapies.* Prog Biophys Mol Biol, 106 (2), 450 – 462.

[91] Scianna, M., Preziosi, L., 2010. *Multiscale Developments of the Cellular Potts Model.* Submitted.

[92] Serini, G., Ambrosi, D., Giraudo, E., Gamba, A., Preziosi, L., Bussolino, F., 2003. *Modeling the early stages of vascular network assembly.* EMBO J, 22 (8), 1771 - 1779.

[93] Sneyd, J., Keizer, J., Sanderson, M. J., 1995. *Mechanisms of calcium oscillations and waves: a quantitative analysis.* FASEB J, 9 (14), 1463 - 1472.

[94] Sneyd, J., Keizer, J., 2009. *Mathematical Physiology.* In Interdisciplinary Applied Mathematics Series, Springer.

[95] Steinberg, M. S., 1963. *Reconstruction of tissues by dissociated cells. Some morphogenetic tissue movements and the sorting out of embryonic cells may have a common explanation.* Science, 141, 401 – 408.

[96] Steinberg, M. S., 1970. *Does differential adhesion govern self-assembly processes in histogenesis? Equilibrium configurations and the emergence of a hierarchy among populations of embryonic cells.* J Exp Zool, 173 (4), 395 – 433.

[97] Takai, Y., Sasaki, T., Matozaki, T., 2001. *Small GTP-binding proteins*. Physiol Rev, 81 (1), 153 - 208.

[98] Tomatis, C., Fiorio Pla, A., Munaron, L., 2007. *Cytosolic calcium microdomains by arachidonic acid and nitric oxide in endothelial cells.* Cell Calcium, 41 (3), 261 - 269.

[99] Tosin, A., Ambrosi, D., Preziosi, L., 2006. *Mechanics and chemotaxis in the morphogenesis of vascular networks.* Bull Math Biol, 68 (7), 1819 - 1836.

[100] Valant, P. A., Adjei, P. N., Haynes, D. H., 1992. *Rapid Ca2+ extrusion via the Na+/Ca2+ exchanger of the human platelet.* J Membr Biol, 130 (1), 63 - 82.

[101] Walther, T., Reinsch, H., Große, A., Ostermann, K., Deutsch, A., Bley, T., 2004. *Mathematical modeling of regulatory mechanisms in yeast colony development.* J Theor Biol, 229 (3), 327 – 338.

[102] Wang, D., Lehman, R. E., Donner, D. B., Matli, M. R., Warren, R. S., Welton, M. L., 2002. *Expression and endocytosis of VEGF and its receptors in human colonic vascular endothelial cells.* Am J Physiol Gastrointest Liver Physiol, 282 (6), 1088 - 1096.

[103] Wang, S., Li, X., Parra, M., Verdin, E., Bassel-Duby, R., Olson, E. N., 2008. *Control of endothelial cell proliferation and migration by VEGF signaling to histone deacetylase 7.* Proc Natl Acad Sci USA, 105 (22), 7738 - 7743.

[104] Wang, N., Tytell, J. D., Ingber, D. E., 2009. *Mechanotransduction at a distance: mechanically coupling the extracellular matrix with the nucleus.* Nat Rev Mol Cell Biol, 10 (1), 75 - 82.

[105] Watson, E. L., Jacobson, K. L., Singh, J. C., DiJulio, D. H., 2004. *Arachidonic acid regulates two Ca2+ entry pathways via nitric oxide.* Cell Signal, 16 (2), 157 - 165.